bioRxiv preprint doi: https://doi.org/10.1101/2023.08.16.553551; this version posted August 17, 2023. The copyright holder for this preprint (which was not certified by peer review) is the author/funder, who has granted bioRxiv a license to display the preprint in perpetuity. It is made available under aCC-BY-NC-ND 4.0 International license.

Control of G protein-coupled receptor function via membrane-interacting intrinsically disordered C-terminal domains

Chiara Mancinelli[1,5], Dagan C. Marx[1,5], Alberto J. Gonzalez-Hernandez[1,5], Lucia Mancinelli[1], George Khelashvilli[2], Joshua Levitz[1,3*], David Eliezer[1,4*]

[1]Department of Biochemistry
[2]Department of Physiology and Biophysics
[3]Department of Psychiatry
[4]Brain and Mind Research Institute
Weill Cornell Medicine, New York, NY 10065, USA

[5] equal contribution

[*] to whom correspondence should be addressed:
Josh Levitz, Department of Biochemistry, Weill Cornell Medicine, New York, NY 10065, 212-746-6565, jtl2003@med.cornell.edu
David Eliezer, Department of Biochemistry, Weill Cornell Medicine, New York, NY 10065, 212-746-6557, dae2005@med.cornell.edu

Preprint Severs: This article was deposited as a preprint in bioRxiv under a CC BY-NC-ND license

Classification: Biological Sciences/Biophysics and Computational Biology

Keywords: GPCR, mGluR, β-arrestin, C-terminal domain, membrane, NMR, disordered protein

bioRxiv preprint doi: https://doi.org/10.1101/2023.08.16.553551; this version posted August 17, 2023. The copyright holder for this preprint (which was not certified by peer review) is the author/funder, who has granted bioRxiv a license to display the preprint in perpetuity. It is made available under aCC-BY-NC-ND 4.0 International license.

Abstract:

G protein-coupled receptors (GPCRs) control intracellular signaling cascades via agonist-dependent coupling to intracellular transducers including heterotrimeric G proteins, GPCR kinases (GRKs), and arrestins. In addition to their critical interactions with the transmembrane core of active GPCRs, all three classes of transducers have also been reported to interact with receptor C-terminal domains (CTDs). An underexplored aspect of GPCR CTDs is their possible role as lipid sensors given their proximity to the membrane. CTD-membrane interactions have the potential to control the accessibility of key regulatory CTD residues to downstream effectors and transducers. Here we report that the CTDs of two closely related family C GPCRs, metabotropic glutamate receptor 2 (mGluR2) and mGluR3, bind to membranes and that this interaction controls receptor function. We first characterize CTD structure with NMR spectroscopy, revealing lipid composition-dependent modes of membrane binding. Using molecular dynamics simulations and structure-guided mutagenesis, we identify key conserved residues and cancer-associated mutations that control CTD-membrane binding. Finally, we provide evidence that mGluR3 transducer coupling is controlled by CTD-membrane interactions in live cells which can be modulated by disease-associated mutations or CTD phosphorylation. This work reveals a novel mechanism of GPCR modulation, suggesting that CTD-membrane binding may be a general regulatory mode throughout the broad GPCR superfamily.

Significance Statement:

G protein-coupled receptors (GPCRs) allow cells to sense and respond to their environment and constitute the largest class of targets for approved therapeutic drugs. Temporally precise GPCR signaling is achieved by coupling the binding of extracellular ligands to the binding of intracellular signal transducers (e.g. heterotrimeric G proteins) and regulators (e.g. β-arrestins). The C-terminal domains (CTDs) of GPCRs are targets of various post-translational modifications and play a critical role in transducer and regulator recruitment. Here we report novel interactions of the CTDs of two GPCRs of the metabotropic glutamate receptor family with cellular membranes. These interactions serve to regulate CTD accessibility and thus, mGluR coupling to transducers and regulators. We propose that dynamic CTD-membrane interaction constitutes a general mechanism for regulating GPCR function.

bioRxiv preprint doi: https://doi.org/10.1101/2023.08.16.553551; this version posted August 17, 2023. The copyright holder for this preprint (which was not certified by peer review) is the author/funder, who has granted bioRxiv a license to display the preprint in perpetuity. It is made available under aCC-BY-NC-ND 4.0 International license.

Introduction:

G protein-coupled receptors (GPCRs) respond to extracellular stimuli to drive intracellular signal transduction pathways that control a wide variety of biological functions. Consistent with their widespread physiological roles, GPCRs also serve as a major class of targets for disease intervention[1,2]. All GPCRs share a conserved architecture including an N-terminal extracellular domain (ECD) of variable size, a seven-helix transmembrane domain (TMD) and an intracellular C-terminal domain (CTD). Signaling is initiated by binding of extracellular ligands to the receptor ECD and/or TMD, inducing conformational changes that control coupling of receptor TMD and CTD to intracellular transducers, including heterotrimeric G proteins, GPCR kinases (GRKs) and β-arrestins (β-arrs).

GPCR CTDs are generally considered to be disordered, consistent with their absence from most structures determined by X-ray crystallography or cryo-EM. Indeed, well-defined conformations, typically limited to small segments of GPCR CTDs, have been captured at high resolution in only a handful of complexes that feature CTD-G protein[3-5] or CTD-arrestin[6-12] interactions, while several recent studies of isolated or unbound CTDs have confirmed their disordered nature[13-16]. In addition to their roles in direct interaction with transducers, the proximity of GPCR CTDs to the membrane may also promote direct interactions with phospholipids. Indeed, membrane binding has been observed for the isolated CTD of the cannabinoid receptor 1[17], and many GPCR CTDs are palmitoylated[18], but the functional implications of CTD-membrane interactions are unclear. CTD-membrane interactions could influence receptor interactions and conformation and thereby modulate receptor ligand binding, activation, and trafficking. Furthermore, such interactions could be sensitive to lipid composition, providing one avenue by which lipids could dynamically regulate receptor function. Along these lines, recent work has demonstrated that reconstituted GPCR activity can be tuned by interactions with specific lipids[19-21], and that β-arr can also directly interact with the lipid bilayer in its receptor-bound state[11,22-24].

Metabotropic glutamate receptors (mGluRs) are dimeric, family C GPCRs that are characterized structurally by their large ECDs which contain a ligand binding domain (LBD) that senses the neurotransmitter glutamate and a cysteine-rich domain that connects the LBD to the TMD (**Fig. 1A**)[25]. Despite this unique ECD arrangement, upon glutamate binding by the LBD, mGluRs couple to G proteins via their TMD in a manner generally analogous to, yet distinct in detail from, that of other GPCR families[5,26-28]. As with other GPCRs, the CTDs of mGluRs are known to be major determinants of their interactions with transducers and regulatory factors[29-32]. Notably, we recently found that modest differences in CTD composition control the ability of the highly homologous group II mGluRs, mGluR2 and mGluR3, to recruit β-arrs[33]. mGluR3 is

bioRxiv preprint doi: https://doi.org/10.1101/2023.08.16.553551; this version posted August 17, 2023. The copyright holder for this preprint (which was not certified by peer review) is the author/funder, who has granted bioRxiv a license to display the preprint in perpetuity. It is made available under aCC-BY-NC-ND 4.0 International license.

efficiently phosphorylated by GRKs and recruits β-arrs, which initiate clathrin-mediated receptor endocytosis, while mGluR2 largely eludes β-arrs driven internalization. This difference is encoded in a short ~20 residue serine/threonine (S/T) rich region of the CTD that begins ~15 residues after the end of TMD helix 7[33].

The central role of the CTD in subtype-specific mGluR regulation raises the question of its structural properties and whether its proximity to the membrane may shape its structure or function. Despite recent cryo-EM studies which have resolved the structures of mGluR ECDs and TMDs in inactive and active states[5,28,34-36], structural information on group II mGluR CTDs is limited to a short membrane-proximal segment of the mGluR2 CTD (residues 821 to 830) which was observed bound to G protein in a recent report[5]. Here, we examine the structural properties and membrane-interactions of the CTDs of mGluR2 and mGluR3. Using a combination of spectroscopic and computational approaches we find that both mGluR2 and mGluR3 CTDs are intrinsically disordered but are capable of interaction with phospholipid membranes. We show that both TMD-proximal and -distal basic residues can mediate electrostatic interactions with lipid headgroups. Additionally, we identify in mGluR3 a critical aromatic residue, Y853, that can stably embed itself in the membrane to potentially restrict access to the mGluR3 CTD S/T-rich. We then find that point mutations, including those associated with melanoma, can modulate membrane interactions, β-arr-dependent internalization, and G protein activation in cells. Furthermore, we show that EGF stimulation leads to agonist-independent mGluR3 internalization, depending on the presence of Y853, suggesting that Y853 phosphorylation drives receptor internalization by releasing the CTD from the membrane. Together this work reveals a complex and dynamic interactions between the intrinsically disordered CTD and the membrane, expanding the known repertoire of GPCR regulatory mechanisms.

Results:

Disordered mGluR CTDs bind negatively charged membranes *in vitro*

To investigate the structure of mGluR CTDs and probe potential membrane interactions, we turned to nuclear magnetic resonance (NMR) spectroscopy using purified, recombinant CTD constructs. For a quantitative, single-residue resolution assay of membrane binding, we took advantage of the effects of the slow tumbling rates of large unilamellar vesicles (LUVs) on NMR signals. Briefly, IDP interactions with vesicles attenuates the signals of residues that interact with the membrane because they adopt the slow tumbling rates and long rotational correlation times

bioRxiv preprint doi: https://doi.org/10.1101/2023.08.16.553551; this version posted August 17, 2023. The copyright holder for this preprint (which was not certified by peer review) is the author/funder, who has granted bioRxiv a license to display the preprint in perpetuity. It is made available under aCC-BY-NC-ND 4.0 International license.

of the LUVs (**Fig. 1B**). This assay has been used extensively to characterize IDP/membrane interactions[37-39] but has not been applied to GPCR CTDs. We first obtained 2D ^{15}N-^{1}H HSQC spectra for both mGluR2 and mGluR3 CTDs in the absence of lipids, which exhibited the sharp signals and limited dispersion that are characteristic of IDPs (**Figs. 1C,D**). In the presence of LUVs composed of DOPS (18:1 1,2-dioleoyl-sn-glycero-3-phospho-L-serine) many signals in the spectra of both CTDs were clearly attenuated (**Figs. 1C,D insets**), indicative of an interaction between the corresponding CTD regions and the negatively charged vesicles. Spectra acquired in the presence of LUVs comprised of 1:1 DOPS:DOPC (18:1 [Δ9-Cis] 1,2-dioleoyl-sn-glycero-3-phosphocholine) or only DOPC exhibited variable degrees of signal loss (**Fig. S1**) suggesting that CTD-membrane interactions are sensitive to lipid composition.

We then asked whether the mGluR CTDs form helical secondary structure upon membrane binding using circular dichroism (CD) spectroscopy. CD spectra of the mGluR2 (**Fig. S2A**) and mGluR3 (**Fig. S2B**) CTDs showed no evidence for alpha-helix formation either in the absence of lipids or in the presence of vesicles under conditions where maximal membrane binding was observed by NMR. Because formation of short segments of helical structure can be difficult to detect in longer polypeptides, we also examined CD spectra of shorter mGluR2 and mGluR3 CTD peptides corresponding more closely to just their membrane-binding regions (see below). These spectra (**Figs. S2C,D**) also showed no evidence for alpha-helix formation in the absence or presence of membranes. Even the presence of membrane mimetic SDS and DPC micelles, which often induce helical structure[40-42], did not result in helix formation (**Figs. S2E**). As a control, we confirmed using CD that LUVs induce robust helical structure in a helix-8 peptide from NTS1 (**Fig. S2F**), as previously reported[43]. These results are consistent with the physico-chemical characteristics of the membrane-binding regions of the mGluR2 and mGluR3 CTDs, which do not show the amphipathic nature typical of membrane-induced helices (see helical wheel plots in **Fig. S2G,H**). Thus, it appears that group II mGluR CTDs remain disordered upon membrane binding.

Electrostatics mediate mGluR CTD-membrane interactions

To enable sequence-specific analysis of CTD-membrane binding, we obtained NMR backbone resonance assignments using conventional triple resonance NMR experiments (**Figs. 1; S1**). Chemical shift based secondary structure assessments confirmed the highly disordered nature of both CTDs in the absence of LUVs, as indicated by the lack of any significant secondary structure propensities (**Figs. S3A,B**). Plots of the ratio of NMR signal intensities in the presence versus absence of LUVs as a function of position (**Figs. 2A,B**) show that both mGluR CTDs

bioRxiv preprint doi: https://doi.org/10.1101/2023.08.16.553551; this version posted August 17, 2023. The copyright holder for this preprint (which was not certified by peer review) is the author/funder, who has granted bioRxiv a license to display the preprint in perpetuity. It is made available under aCC-BY-NC-ND 4.0 International license.

interact with phospholipids via their N-terminal regions. For both CTDs, NMR signal attenuation is dependent on negatively charged lipid content, as signal attenuation is absent (mGluR2) or decreased (mGluR3) in the absence of DOPS (**Figs. 2A,B; S1**). Despite similar binding profiles at their N-termini, the membrane binding region for the mGluR3 CTD is longer, spanning the first ~30 residues, compared with ~21 residues for mGluR2. Plots of the average intensity ratio as a function of LUV composition within the N-terminal 20 residues (**Fig. 2C**) illustrate both the clear DOPS-dependence of membrane binding in this region, in contrast with the C-terminal region (**Fig. 2D**)

Inspection of the sequence of both mGluR CTDs revealed a conserved N-terminal cluster of basic residues (**Fig. 3A**), which we hypothesized could drive CTD binding to negatively charged DOPS headgroups. Mutagenesis of each of the four basic residues in this cluster to alanine reduced membrane binding for the mGluR2 CTD, with the strongest effect observed for R834A (**Figs. 3B,C; S4**). The effect was most pronounced for LUVs composed of 1:1 DOPS:DOPC, indicating that increasing negative charge content in the membrane can partly compensate for the loss of individual basic residues in the CTD (**Fig. 3C**). These results support a major role for electrostatic interactions between basic CTD residues and anionic phospholipids in driving CTD-membrane interactions.

To further understand the properties of the mGluR CTD-membrane interaction, we examined the potential role of membrane curvature in altering the membrane-bound region of mGluR CTD. We measured binding to DOPS vesicles with diameters ranging from 50-400 nm and observed no substantial changes in mGluR2 membrane binding, indicating that mGluR CTDs are insensitive to membrane curvature (**Fig. S5**). To assess whether different regions of the protein are bound to the membrane with different affinities, we obtained NMR intensity ratio data for the mGluR3 CTD as a function of lipid concentration (**Fig. S6)**. We find that the N-terminal basic cluster remains bound even at lower lipid concentrations but observe a reduction in binding of the subsequent residues (S845 to T860) comprising the S/T-rich region of the mGluR3 CTD, suggesting that this region binds more weakly.

An aromatic residue anchors the mGluR3 CTD S/T-rich region to the membrane

To further probe structural changes in the mGluR CTDs upon binding to membranes, we turned to all-atom molecular dynamics simulations. We focused our analysis on the mGluR3 CTD, as this subtype features more extensive membrane interactions than mGluR2 (**Figs. 2**), and since the CTD is known to have a central role in mGluR3 regulation[33]. We built a system containing a 1:1 DOPC/DOPS phospholipid bilayer and a protein chain comprising both transmembrane helix

bioRxiv preprint doi: https://doi.org/10.1101/2023.08.16.553551; this version posted August 17, 2023. The copyright holder for this preprint (which was not certified by peer review) is the author/funder, who has granted bioRxiv a license to display the preprint in perpetuity. It is made available under aCC-BY-NC-ND 4.0 International license.

7 (TM7) of mGluR3 and the CTD (*see Methods*). We included the transmembrane tether to increase the probability of observing CTD-membrane interactions within the simulation time and to bridge the *in vitro* experiments with isolated CTDs to the biological context of the CTD where it is attached to the TMD at its N-terminus. We started the simulations with the CTD in a disordered conformation with no contacts with the membrane and 6 independent replicas were simulated for ~375 ns each, resulting in ~2.25 μs of total simulation time (**Figs. S7A-F**). In all replicas, we observed interactions between the mGluR3 CTD and the membrane. We did not observe any alpha-helix formation and found instead that the mGluR3 CTD is conformationally dynamic with little or no regular secondary structure (**Figs. S7A-F,** panels iii), consistent with our CD data above (**Fig. S2**).

Since our NMR-based binding profiles revealed an extended membrane binding interface for the mGluR3 CTD, we sought to identify trajectories that captured a similar membrane binding mode. We calculated the distance of each C_α in the CTD from the lipid phosphate plane to assess CTD-membrane interactions on a residue-by-residue basis and facilitate comparison with our NMR data (**Fig. S7**, panels ii). We find that all the trajectories exhibit proximity of the N-terminal basic cluster region to the membrane surface, consistent with the tighter binding observed for this region in our NMR experiments. Furthermore, one of the trajectories, replica 6 (**Fig. S7F,** panel ii), featured a more extended membrane binding region, encompassing the N-terminal ~28 residues, that agrees well with the NMR data at high lipid concentrations, suggesting that the binding mode captured in this simulation is consistent with that observed *in vitro* (**Figs. 4A,B**). We also calculated the radius of gyration (R_g) of the CTD during each trajectory to determine its hydrodynamic size. Four of the six trajectories (replicas 1-4) primarily sample more compact conformations of the CTD (**Figs. S8A,B**) which do not bind the membrane. The two remaining trajectories (replicas 5 and 6) sample more extended conformations, with replica 5 exhibiting proximity of the N-terminal basic cluster to the membrane, matching our NMR data at lower lipid concentrations (**Fig. S8C**). For both replica 5 and 6, interactions between basic residues (primarily R838 and R843) and DOPS headgroups (**Figs. 4C; S8D-G**) anchor the N-terminal region to the membrane. We also found that dynamic interactions between R869 and the membrane contribute to transient anchoring of the C-terminal portion of the CTD to the bilayer (**Figs. 4A; S8D-G**).

The extended mGluR3-CTD binding region observed in replica 6 includes the S/T-rich region (**Fig**. **5A**) which we have shown confers β-arr-mediated internalization[33]. Intriguingly, Y853 within this region shows the largest buried surface area in replica 6 (**Figs. 4C; 5B,C**), which captures the extended binding mode, but is situated far from the membrane in replica 5 (**Fig. S8C**). Aromatic residues are known to partition favorably into membranes and are often found in

bioRxiv preprint doi: https://doi.org/10.1101/2023.08.16.553551; this version posted August 17, 2023. The copyright holder for this preprint (which was not certified by peer review) is the author/funder, who has granted bioRxiv a license to display the preprint in perpetuity. It is made available under aCC-BY-NC-ND 4.0 International license.

interfacial regions of transmembrane domains[44-46]. Accordingly, Y853 was consistently found either inserted into the membrane or at the interfacial lipid headgroup region in replica 6 (**Figs. 5B,C**). Furthermore, the membrane proximity of nearby S/T residues appears to be correlated with that of Y853 (**Fig. S9A**), while remaining dynamic (**Fig. S9B**). To further probe the importance of this aromatic residue in the membrane interactions of the S/T-rich region of the mGluR3 CTD, we examined the effects of mutating Y853 to alanine using our NMR-based assay. Compared to WT, Y853A resulted in a similar binding profile to 1:1 DOPC:DOPS vesicles for the N-terminal basic region, but showed decreased binding of the CTD in the S/T-rich region (**Figs. 5D; S9C,D**). Indeed, the resulting profiles resemble those obtained at lower lipid concentrations, indicating that Y853 plays a crucial role in stabilizing the extended binding mode seen in replica 6 and at higher lipid concentrations.

CTD-membrane binding is modulated by cancer-associated mutations.

The mGluR3 CTD contains a number of cancer-associated mutations, two of which, G848E and E870K, are frequently observed in melanomas[47]. G848 lies within the S/T-rich region, nestled in between R843 and Y853, and is membrane-associated according to both the NMR data and our MD simulations (**Figs. 4B; 5E,F**). E870 is in the C-terminal region of the mGluR3 CTD that is weakly membrane associated according to the NMR data and features transient contacts with the membrane in our simulation that are likely mediated by its neighbor R869 (**Figs. 5E,F**). Based on these results, we hypothesized that both cancer-associated mutations could alter membrane binding due to changes in the local electrostatic properties of the mGluR3 CTD that would either diminish (G848E) or promote (E870K) interactions with DOPS headgroups. To test this, we measured binding of these mutants using our NMR-based approach. The mGluR3 CTD G848E variant resulted in reduced interaction between the S/T-rich region of the CTD and the membrane, similar to the effect observed for the Y853A mutation (**Figs. 5G; S9C,D**). Strikingly, the E870K mutation extended the membrane-interacting region of the CTD nearly to its very C-terminus (**Figs. 5H; S9C,D**). The ability of both cancer-associated mutations to alter CTD-membrane binding further supports the role of electrostatics in driving these interactions.

mGluR3 CTD membrane interactions modulate receptor internalization in living cells

Having established that mGluR3 mutations can alter membrane binding *in vitro*, we next asked if modifications which alter CTD-membrane interactions can also alter receptor function in living cells. We initially focused on agonist-induced mGluR3 internalization, which is driven by phosphorylation-dependent interactions with β-arrs[33]. As described above, we reasoned that

bioRxiv preprint doi: https://doi.org/10.1101/2023.08.16.553551; this version posted August 17, 2023. The copyright holder for this preprint (which was not certified by peer review) is the author/funder, who has granted bioRxiv a license to display the preprint in perpetuity. It is made available under aCC-BY-NC-ND 4.0 International license.

binding of the mGluR3 S/T-rich region to the membrane surface could modulate the ability of the CTD to interact with GRKs and/or β-arrs to mediate internalization.

We assessed the effects of the Y853A, G848E, and E870K mutations (**Fig. 6A**) on mGluR3 internalization using an established live cell surface labeling imaging-based assay[33]. All mutants expressed on the surface, although a small decrease relative to wild type was observed for G848E and E870K (**Fig. S10A**). To quantify receptor internalization, we labeled N-terminal SNAP-tagged mGluR3 transfected into HEK 293T cells with a membrane-impermeable fluorophore after 60 min treatment with agonist or antagonist. A consistent ~30% drop in fluorescence was observed for wild type mGluR3 following agonist treatment, reflecting endocytosis (**Fig. 6B**). Compared to WT, G848E and Y853A mGluR3 mutants exhibit a greater degree of glutamate-evoked internalization (**Fig. 6B**). The data for G848E are consistent with our previous report that this mutation results in enhanced internalization[33]. In contrast, the E870K mutation drastically decreased glutamate-induced internalization of mGluR3 (**Fig. 6B**). These results are consistent with our hypothesis that CTD-membrane interactions regulate the accessibility of the CTD to GRKs and β-arrs, with mutations that inhibit or enhance CTD-membrane binding exhibiting enhanced or blunted internalization, respectively.

To further assess our interpretation that altered CTD-membrane interactions underlie the observed changes in receptor internalization, we examined the effects of artificially anchoring the mGluR3 CTD to the membrane by appending a CAAX box lipidation motif to its C-terminus (**Figs. 6A; S10A**). Indeed, this variant exhibited a reduction in glutamate-induced receptor internalization similarly to the E870K mutant receptor (**Fig. 6B**). We also visualized receptor internalization via live cell microscopy where we labeled plasma membrane SNAP-tagged mGluR3 variants with a membrane-impermeable fluorophore and visualized fluorescence localization following glutamate treatment (30 min, 1 mM). This analysis confirmed the enhanced internalization of G848E and Y853A and the reduced internalization of E870K and mGluR3-CAAX following either 15 or 60 min of glutamate treatment (**Fig. 6C**).

To assess any effects of CTD mutations on G protein activation, we performed patch clamp measurements using a GIRK channel current assay (see Methods). In this assay, G848E showed a clear left-shift and Y853A showed a small right-shift, while E870K and -CAAX showed similar apparent glutamate affinities to wild type mGluR3 (**Figs. 6D; S10B,C**). These observations suggest that these mutations can exert distinct functional effects on β-arr and G protein coupling.

Motivated by our observations of the key contribution of residue Y853 to the membrane interactions of the mGluR3 CTD S/T-rich region, we considered whether phosphorylation of this residue could influence CTD-effector interactions by reducing membrane binding. Consistent with

bioRxiv preprint doi: https://doi.org/10.1101/2023.08.16.553551; this version posted August 17, 2023. The copyright holder for this preprint (which was not certified by peer review) is the author/funder, who has granted bioRxiv a license to display the preprint in perpetuity. It is made available under aCC-BY-NC-ND 4.0 International license.

this hypothesis, a phosphomimetic Y853D mutant showed enhanced internalization compared to WT (**Fig. 6E**). We then found that treatment of mGluR3-transfected HEK 293T cells with epidermal growth factor (EGF; 100 ng/ml), which stimulates myriad downstream kinase signaling pathways, led to detectable internalization of WT, but not of Y853A mGluR3 in the absence of agonist (**Figs. 6F,G**). Combining agonist and EGF treatment enhanced internalization to a similar extent to that observed for the agonist treated Y853A mutant (**Fig. 6G**). These results suggest that membrane-interacting residues in the mGluR3 CTD can contribute to both agonist-driven homologous internalization and heterologous internalization following stimulation of other cellular pathways.

Discussion:

Many transmembrane proteins contain disordered intracellular domains in the form of either extended loops or terminal domains that frequently serve important scaffolding roles to control localization/trafficking and are typically regulated by phosphorylation or other post-translational modification. However, a structural understanding of such domains is often limited as they are rarely resolved in X-ray crystallography or cryo-EM studies. The functional roles of disordered intracellular domains in GPCRs, particularly their CTDs, have drawn increasing interest in recent years. Several studies have confirmed the disordered nature of GPCR CTDs[13-16] and direct interactions of receptor CTDs with the intracellular face of the corresponding TMDs, which are regulated by phosphorylation and/or agonist binding and influence both receptor activity and coupling to β-arrs, have been documented[15,16,48]. In addition to their scaffolding and autoinhibitory interactions, direct binding of disordered intracellular domains to the membrane has been shown to play functional roles[49-51], but GPCRs have not been the subject of such studies to date. Membrane phospholipid composition and cholesterol levels have been shown to modulate GPCR function[20,21], but this has been thought to occur primarily by direct interactions with membrane-embedded TMDs. Here, we show that GPCRs can also sense the membrane in a functionally relevant way through their disordered intracellular CTDs. Specifically, we find that the CTDs of family C GPCRs mGluR2 and mGluR3 interact with membranes via electrostatic and hydrophobic interactions and that modulating CTD-membrane interactions by de novo or cancer-associated mutations alters receptor internalization.

CTDs of mGluR2 and mGluR3 bind to membranes without adopting secondary structure.

bioRxiv preprint doi: https://doi.org/10.1101/2023.08.16.553551; this version posted August 17, 2023. The copyright holder for this preprint (which was not certified by peer review) is the author/funder, who has granted bioRxiv a license to display the preprint in perpetuity. It is made available under aCC-BY-NC-ND 4.0 International license.

We recently reported that mGluR3, but not mGluR2, couples strongly to β-arrs, dependent on the presence of an S/T-rich region in its CTD[33]. Here we used NMR spectroscopy to show that both CTDs are highly disordered in solution and bind to unilamellar lipid vesicles via their N-terminal regions, with the mGluR3 membrane-binding region extending further than that of mGluR2 to encompass the S/T-rich region. While many disordered protein regions that interact with membranes adopt amphipathic helical structure upon binding, including the short amphipathic membrane-associated helix-8 of many GPCRs[43], our CD data and MD simulations demonstrate that the mGluR2 and mGluR3 CTDs do not form detectable helical structure upon membrane binding. This is consistent with recently reported cryo-EM structures of full-length mGluR2 and mGluR3 which do not feature a classical helix 8[5,52]. Notably, our data do not rule out the possibility of very short helical segments in the membrane-bound CTDs, which have been observed in other intracellular membrane-binding domains[49].

Consistent with our findings for the mGluR CTDs, there are numerous examples of IDP-membrane interaction modes that do not involve secondary structure formation. A prominent example is the MARCKS-ED peptide from the effector domain of myristoylated alanine-rich C-kinase substrate[53,54], which features 13 positively charged and 5 hydrophobic residues within a short 25-residue polypeptide segment. The C-terminal motif of worm complexin also binds to membranes without secondary structure via a combination of positively charged and hydrophobic side chains[55,56]. Another particularly relevant example is the N-terminal region of the *Mycobacterium tuberculosis* divisome protein ChiZ, which binds to acidic membranes primarily via hydrogen bonds between phospholipid headgroups and 9 arginine residues[57].

mGluR3-transducer coupling is modulated by CTD-membrane interactions

We posit that CTD-membrane interactions can regulate CTD availability for interactions with downstream effectors such as GRKs and β-arrs. We utilized two cancer-associated mutations and one de novo mutation in the mGluR3 CTD to demonstrate an inverse correlation between membrane binding of the mGluR3 S/T-rich region and β-arr-mediated receptor internalization in living cells. Mutations that reduce local membrane association (G848E and Y853A) result in increased receptor internalization, whereas a mutation that enhances and extends membrane binding (E870K) results in increased receptor internalization. Importantly, introduction of a membrane anchoring CAAX box motif at the C-terminus of mGluR3 also decreases receptor internalization and further strengthens the relationship between CTD-membrane binding and receptor internalization.

bioRxiv preprint doi: https://doi.org/10.1101/2023.08.16.553551; this version posted August 17, 2023. The copyright holder for this preprint (which was not certified by peer review) is the author/funder, who has granted bioRxiv a license to display the preprint in perpetuity. It is made available under aCC-BY-NC-ND 4.0 International license.

Tyr phosphorylation can complement Ser/Thr phosphorylation in GPCR CTDs

The presence of Y853 within the S/T-rich region and its importance for the membrane interactions of this region prompted us to consider the possibility that phosphorylation of this tyrosine residue could also play a role in modulating CTD-membrane binding, and thereby regulating coupling to transducers, including β-arrs. Notably, tyrosine residues are known to partition favorably at membrane/water interfaces and have been observed to anchor the membrane interactions of other disordered intracellular domains[49], and tyrosine phosphorylation has previously been reported to disrupt localized membrane binding of several disordered proteins[58,59]. Indeed, we found that treatment of cells expressing mGluR3 with EGF resulted in mGluR3 internalization even in the absence of agonist, and enhanced internalization in the presence of agonist, dependent on the presence of Y853. Introducing the phosphomimetic Y853D mutation also enhanced agonist-stimulated mGluR3 internalization. Together these observations support a potential role for Y853 phosphorylation-induced release of the mGluR3 CTD from the membrane, increasing its accessibility for GRK and β-arr coupling. In light our own observations of the role of tyrosine-membrane interactions in regulating mGluR3 internalization and previous reports of their role in regulating T cell receptor activation[49], we posit that modulation of such interactions may constitute a general mechanism for receptor regulation.

GPCR CTDs influence receptor function via multiple modalities.

The work presented here makes a case for a general role for GPCR CTD-membrane interactions in regulating the accessibility of receptor CTDs to downstream effectors, including β-arrs. Our data and simulations are consistent with a model where the CTD exists in an equilibrium between membrane-bound and membrane-free states which can be modulated by receptor activation, transducer binding, post-translational modifications and changes in membrane composition (**Fig. 6H**). An appealing aspect of this model is that it provides a mechanism for sequential or cooperative phosphorylation[60] as initial phosphorylation events could shift the equilibrium of phosphocode-containing regions[9,61] and increase their accessibility for further phosphorylation and subsequent β-arr binding.

Together with recent results describing functionally important interactions of receptor CTDs with the intracellular face of their TMDs[15,16,48], our work expands the modalities by which GPCR CTDs can regulate receptor function. Several important questions emerge, perhaps the most compelling of which is how the interplay of CTD interactions with membranes, TMDs, G-proteins, GRKs, β-arrs and other effectors is regulated and orchestrated. For example, we observe that two mGluR3 mutations, G848E and Y853A, that exert similar effects on CTD-

bioRxiv preprint doi: https://doi.org/10.1101/2023.08.16.553551; this version posted August 17, 2023. The copyright holder for this preprint (which was not certified by peer review) is the author/funder, who has granted bioRxiv a license to display the preprint in perpetuity. It is made available under aCC-BY-NC-ND 4.0 International license.

membrane interactions and on receptor internalization exhibit opposite effects in an assay of receptor activation, suggesting additional effects beyond membrane binding. Similarly, the G848E and E870K mutations affect CTD-membrane interactions in opposite ways, yet both mutations are found in melanomas, suggesting that their effects extend beyond those observed here. Effects on G-protein recruitment via direct CTD G-protein binding[3-5], autoinhibitory CTD interactions with G-protein binding sites on the TMD[15,33,48], or allosteric effect on TMD conformation may be responsible. Indeed, we recently reported an auto-inhibitory effect of the mGluR2 CTD on β-arr coupling[33], supporting a potential interplay between TMD- and membrane-binding. A recent study of the calcium sensing receptor (CaSR) also proposed a potential interplay between sequestration of a short CTD segment and its interactions with G-proteins[62]. Phosphorylation likely plays a role in regulating each type of CTD interaction, but understanding the net effects of modulating each individual interaction will require novel approaches. While our focus here has been on the CTD, similar mechanisms and interactions may be operative for other disordered intracellular GPCR domains[63]. Beyond integrating the effects of multiple CTD interactions, an additional subject for investigation is whether and how these interactions, individually or in sum, influence receptor conformation and activation directly via allosteric coupling between CTD conformations and interactions and the TMD.

Conclusions

Our results establish a previously unappreciated yet critical and dynamic role of CTD membrane interactions in controlling GPCR desensitization and internalization and suggest that an equilibrium between membrane-bound and free states controls transducer coupling efficiency. This equilibrium may be modified in multiple ways, including disease mutations, Ser/Thr phosphorylation and possibly Tyr phosphorylation, as well as changes in membrane composition, comprising a novel mode of CTD-mediated GPCR regulation.

bioRxiv preprint doi: https://doi.org/10.1101/2023.08.16.553551; this version posted August 17, 2023. The copyright holder for this preprint (which was not certified by peer review) is the author/funder, who has granted bioRxiv a license to display the preprint in perpetuity. It is made available under aCC-BY-NC-ND 4.0 International license.

Methods:

Protein expression and purification

Plasmids encoding the rat mGluR2 (residues 821-872) and mGluR3 (residues 830-879) CTDs preceded by an N-terminal 6x-His-SUMO tag were procured from Twist Biosciences. Cysteine-free versions of both mGluR2 (C859A) and mGluR3 (C866A) were generated using an In-Fusion Cloning kit (Takara Bio) and confirmed by DNA sequencing, and were used as the background for generating the other mutants described. In each case, a conserved proline located at the end of TM7[28,64] was selected as the start of the CTD. Recombinant proteins were expressed in *E. coli* BL21/DE3 cells (Novagen) grown in either LB Broth or M9 minimal media containing ^{15}N-labeled ammonium chloride (1 g/L) or ^{15}N-labeled ammonium chloride and ^{13}C-labeled D-glucose (2 g/L) at 37 ° C (275 rpm) induced with 1 mM IPTG (Isopropyl β-D-1-thiocalactopyranoside) at OD_{600nm} of 0.6-0.8. 4 hours post induction, cells were harvested via centrifugation at ca. 10,500 g at 4°C for 15 mins. Cell pellets (stored at -20°C overnight) were resuspended in 50 mL lysis buffer (350mM NaCl, 20 mM Imidazole, 20 mM Tris pH 8.0, 1mM PMSF, 1 mM EDTA and 3 mM βME) and lysed either via sonication on ice for 3 rounds of 6 mins, 50% duty cycle or using an EmulsiFlex-C3 (AVESTIN, Ontario, Canada), followed by centrifugation at ca. 40,000 g for 1 hour to remove cellular debris. The supernatant was loaded onto a Ni-NTA column equilibrated using 350 mM NaCl, 20 mM Imidazole, 20 mM Tris pH 8.0, 3 mM βME, washed with the same buffer and the SUMO-tagged protein was eluted using 350 mM NaCl, 250 mM Imidazole, 20 mM Tris pH 8.0, 3 mM βME. Protein-containing fractions were pooled and cleaved overnight using SUMO protease (added to final concentration ca. 1 μM), followed by dialysis against 150 mM NaCl, 20 mM Tris pH 8.0, and 1mM DTT and loaded again onto a Ni-NTA column. The cleaved CTDs were collected in the flowthrough and further purified over a 5 mL HiTrap™ SP HP column on an AKTA Pure Protein Purification System (GE). Purified CTDs were either dialyzed into ddH_2O, flash frozen and lyophilized (mGluR2) or exchanged into NMR Buffer (100 mM NaCl, 10 mM Na_2HPO_4 at pH 6.8) by overnight dialysis or using a PD-10 Column (Cytiva, Marlborough, MA) (mGluR3) and concentrated as necessary using 3K MWCO Amicon Ultra Centrifugal filters (Millipore Sigma, Darmstadt, Germany) at 10°C. Lyophillized mGluR2 CTD was resolubilized to ca. 250 uM (by weight) stock concentration in NMR Buffer.

Large unilamellar vesical (LUV) preparation

18:1 1,2-dioleoyl-sn-glycero-3-phospho-L-serine (DOPS) and 18:1 [Δ9-Cis] 1,2-dioleoyl-sn-glycero-3-phosphocholine (DOPC) were purchased from Avanti Polar Lipids (Alabaster, AL)

bioRxiv preprint doi: https://doi.org/10.1101/2023.08.16.553551; this version posted August 17, 2023. The copyright holder for this preprint (which was not certified by peer review) is the author/funder, who has granted bioRxiv a license to display the preprint in perpetuity. It is made available under aCC-BY-NC-ND 4.0 International license.

dissolved in chloroform and stored at -20 ° C. Lipids were mixed to desired ratios (100% DOPS, 1:1 DOPS: DOPC and 100% DOPC), residual solvent was removed under vacuum for 1-2 hours, and lipids were then stored under N_2(g) at -20 ° C. Lipids were resuspended to 20 mM (total lipid concentration) in 1 mL using either NMR buffer and subjected to 10 freeze/thaw cycles using liquid nitrogen/warm water baths. LUVs were then prepared using a 1 mL Avanti Mini-Extruder (Avanti Polar Lipids) by extruding 21 times using either a 100 nm (for NMR) or 50 nm (for CD) pore size polycarbonate film. Smaller diameter LUVs were used for CD to limit scattering at lower wavelengths that was apparent in data collected for the mGluR3 CTD using NMR samples prepared with 100 nm LUVs (**Fig. S2A**). For vesicle size titrations, LUVs were additionally extruded using 400 nm and 200 nm pore size polycarbonate film. LUVs were stored at 4 ° C and used within 5 days.

Nuclear magnetic resonance (NMR) spectroscopy

CTDs were prepared in NMR Buffer as described above at concentrations ranging from ca. 50-150 μM for 5 mm NMR tubes or 300 μM for 1.7 mm NMR tubes with or without 10 mM LUVs. Relative protein concentrations were corroborated by 1D proton NMR using 4,4-dimethyl-4-silapentane-1-sulfonic acid (DSS) as an internal standard. For lipid titrations LUV concentrations included 10, 5 and 2.5 mM. ^{1}H-^{15}N HSQC NMR were collected on a Bruker AVANCE 500-MHz spectrometer (Weill Cornell NMR Core) equipped with a Bruker TCI cryoprobe at 10° C with 1024 complex points in the ^{1}H dimension and 146 complex points in the ^{15}N dimension using spectral widths of 18 PPM (^{1}H) and 24 PPM (^{15}N). NMR spectra were processed using NMRpipe and analyzed using NMRFAM-sparky 3.115 and NMRbox. Intensity ratios were calculated as the ratio of intensities in spectra of samples with LUVs to those of matched free protein samples with no LUVs. Intensity ratios for cysteine-free CTDs were compared to those of WT CTDs (**Fig. S1C,F**). As no meaningful differences were observed, and as the cysteine residues are located outside the membrane-binding regions of both CTDs, the cysteine-free versions were used in all subsequent experiments. To assess the binding of different CTD regions for LUVs of different compositions and size and for CTD mutants, intensity ratios were averaged over the regions of interest.

Backbone resonance assignments were made using standard triple resonance experiments collected on a Bruker Avance III spectrometer at 800 Hz. Assignments were initially obtained for the WT mGluR2 and mGluR3 CTDs and were transferred by inspection for most mutants, but were augmented using HNCA spectra in select cases (mGluR2 C859A and mGluR3

bioRxiv preprint doi: https://doi.org/10.1101/2023.08.16.553551; this version posted August 17, 2023. The copyright holder for this preprint (which was not certified by peer review) is the author/funder, who has granted bioRxiv a license to display the preprint in perpetuity. It is made available under aCC-BY-NC-ND 4.0 International license.

G848E). Secondary Cα shifts were calculated by subtracting reference random coil Cα shifts[65,66] from the observed values.

Circular dichroism (CD) spectroscopy

CD measurements were performed on an AVIV 410 CD spectropolarimeter. Spectra were obtained from 300-190 nm at 25° C after a two-minute temperature equilibration with a wavelength step of 1 nm, an averaging time of 5 seconds, 1 scan per sample and a cell path length of 0.02 cm (Starna, Atascadero, CA). Backgrounds were collected and subtracted from all spectra. Final CTD concentrations ranged from ca. 50-100 μM with protein and peptide stock concentrations estimated by weight, or using A280 with a calculated extinction coefficient of 2980 $M^{-1}cm^{-1}$ for mGluR3 CTD, and also assessed using 1D proton NMR with DSS as an internal standard. WT mGluR 2 and mGluR3 peptides encompassing the first 23 residues of each CTD (mGluR2:PQKNVVSHRAPTSRFGSAAPRAS, mGluR3:PQKNVVTHRLHLNRFSVSGTGTT) were purchased from GenScript (Piscataway, NJ) (>= 95% purity). Peptides were dissolved in NMR buffer at 1 mg/mL and mixed 1:1 with CD buffer or LUVs in CD buffer for a final concentration of 0.5 mg/mL. NTS1 peptide encompassing the first 16 residues of its CTD (SANFRQVFLSTLACLC) purchased from from GenScript (>= 95% purity) was dissolved in 100% trifluoroethanol (TFE) at 15 mgs/ml as previously reported[43] prior to dilution with NMR buffer to 0.4 mg/mL and final 1:1 mixing with buffer or LUVs to a final concentration of 0.2 mg/mL with 0.67% residual TFE. The dearth of aromatic residues in all of the polypeptides used made reliable determination of absolute protein concentrations exceedingly difficult. Therefore, CD data are presented in millidegrees and were not converted to mean residual molar ellipticity.

Molecular dynamics simulations

All-atom molecular dynamics simulations were performed on an mGluR3 construct containing both TM7 and the CTD (residues 796-879). We used AlphaFold2[67] and ColabFold[68] to create models of the mGluR3 TMD and CTD structure because no structures of mGluRs contain a fully resolved CTD. We chose the top ranked of five models (highest average AlphaFold pLDDT score), all of which contained a disordered CTD, and isolated the TM7-CTD residues as our starting structure. CHARMM-GUI[69-75] was used to build a single system of our starting structure embedded in a 1:1 DOPS-DOPC phospholipid bilayer (139 lipids per leaflet), including 104,130 water molecules and 0.2 M NaCl at 37°C. Lysine and histidine residues were protonated to approximate experimental pH.

bioRxiv preprint doi: https://doi.org/10.1101/2023.08.16.553551; this version posted August 17, 2023. The copyright holder for this preprint (which was not certified by peer review) is the author/funder, who has granted bioRxiv a license to display the preprint in perpetuity. It is made available under aCC-BY-NC-ND 4.0 International license.

The initial simulation was equilibrated using the standard CHARMM-GUI based protocol and scripts followed by a short, 6-ns run using OpenMM[76] and the CHARMM36m[77] forcefield. Following this equilibration protocol, velocities for each atom in the system were randomized and used to create 6 statistically independent replicates that were then simulated for 374 ns for a total of ~2.25μs of simulation time.

Analysis of the trajectories was performed using a combination of VMD[78] plug-ins and home-made TCL and python scripts. To determine the position of side chains relative to the phosphate plane, we adapted an approach from Marx and Fleming[79] in which we compared the z-position of a side chain center of mass to the average z-position of the phosphate atoms in the bilayer leaflet closest to the CTD in each frame. The percent burial of side chains in the lipid bilayer was determined by calculating the difference in solvent accessible surface area (SASA), calculated using VMD, for a side chain in the absence and presence of the lipid bilayer for each frame. This approach was used to account for SASA reductions not resulting from lipid interactions. Side chain-lipid hydrogen bonds were calculated with the Hbonds plug-in in VMD using default settings for bond angle and length. HullRad[80,81] was used to calculate the radius of gyration of each frame of the simulation. Secondary structure of each residue was calculated using for each frame using homemade TCL scripts.

Patch clamp electrophysiology

Whole-cell patch clamp recordings were performed in HEK 293 cells 24 hours post-transfection as previously described[82]. Briefly, cells were transfected using Lipofectamine 2000 (Thermo Fisher Scientific) with the wildtype or mutant mGluRs together with GIRK1-F137S[83] and soluble tdTomato as a transfection marker in 1:1:0.2 ratio. Recording pipettes of borosilicate and with 3-5 MΩ resistance were filled with intracellular solution (in mM): 140 KCl, 10 HEPES, 5 EGTA, 3 MgCl2, 3 Na_2ATP, 0.2 Na_2GTP. Cells were clamped at -60 mV in a high-potassium bath solution containing (in mM): 120 KCl, 25 NaCl, 10 HEPES, 2 $CaCl_2$, 1 $MgCl_2$. Glutamate evoked potassium currents were recorded with an Axopatch 200B and Digidata 1550B (Molecular Devices) using Clampex (pCLAMP) acquisition software. Peak currents for the different glutamate concentrations were measured using Clampfit (pCLAMP) and normalized to the maximum current observed at saturating 1 mM glutamate.

Cell imaging and surface labelling assay

To image and quantify the internalization of receptors after glutamate exposure we used N-terminally SNAP-tagged mGluR3 receptors[33]. HEK 293T Cells were transfected with the

bioRxiv preprint doi: https://doi.org/10.1101/2023.08.16.553551; this version posted August 17, 2023. The copyright holder for this preprint (which was not certified by peer review) is the author/funder, who has granted bioRxiv a license to display the preprint in perpetuity. It is made available under aCC-BY-NC-ND 4.0 International license.

wildtype or mutant SNAP-mGluR3s. 24 hrs post-transfection cells were prepared for experiments by labeling tem with 1 μM BG-Surface Alexa 546 (non-permeable dye, New England BioLabs) for 30 min at 37ºC in a media containing (in mM): 10 HEPES, 135 NaCl, 5.4 KCl, 2 $CaCl_2$, 1 $MgCl_2$, pH 7.4. After this, cells were washed twice and incubated with glutamate (1 mM) for 30 min. Cells were then imaged under an Olympus IX83 inverted microscope using a 100X 1.49 NA objective and an Orca-Flash 4.0 CMOS camera (Hamamatsu). Representative images were selected over a minimum of 10 images per condition.

For quantifying internalization after glutamate of the wildtype and mutant receptors we used a previously reported surface labelling assay[33]. Briefly, cells expressing different SNAP-tagged mGluR3 constructs were exposed to 1 mM glutamate, or 20 μM of the antagonist LY341495 (Tocris) for normalization, for 1 hr at 37ºC. Following drug incubation, cells were labelled with 1 μM BG-Surface Alexa 546 for 20 min at room temperature and imaged immediately using a 60x 1.49 NA objective. Images were analyzed using Image J (Fiji). Mean intensity of thresholded fluorescent areas was calculated using a macro based in the Li algorithm. Background of the tresholded images was subtracted and the resultant values were normalized to the antagonist incubated condition, inverted to show amount of internalization (instead of fluorescence drop) and converted to percentage of internalization. These values were averaged per day. Each point of the bar plots represents a day of experiments. For EGF-stimulated internalization we followed the same approach but applying 100 ng/mL of EGF alone or together with 1 mM Glu. Quantification was performed using the same Li algorithm macro and comparisons were made within each condition (EGF or Glu+EGF) for WT vs Y853A mutant.

Data Sharing Plan:

All NMR chemical shift assignments (deposition in progress) can be obtained online from the biological magnetic resonance database (BMRB). NMR intensity and intensity ratio data, CD data, and all code used for the analysis of MD simulations (deposition in progress) can be obtained online at GitHub. Imaging data will be made available upon request, as well all plasmids and reagents used in the study.

Acknowledgments and funding sources:

This work was funded in part by National Institutes of Health (NIH) grants R35GM136686 (DE), R01NS129904 (JL), F32GM148001 (DM), F31AG077836 (CM) and the Margarita Salas Fellowship from the Ministry of Universities of Spain (A.G.-H), the Rohr Family Research Scholar Award (JL), and the Monique Weill-Caulier Award (JL). G.K. gratefully acknowledges support from

bioRxiv preprint doi: https://doi.org/10.1101/2023.08.16.553551; this version posted August 17, 2023. The copyright holder for this preprint (which was not certified by peer review) is the author/funder, who has granted bioRxiv a license to display the preprint in perpetuity. It is made available under aCC-BY-NC-ND 4.0 International license.

the 1923 Fund. We acknowledge assistance from Clay Bracken and Emily Grasso with NMR data collection and processing, Jihye Kim for guidance on EGF stimulation studies and Derek Shore for assistance setting up simulations. The authors gratefully acknowledge the use of in-house computational resources of the David A. Cofrin Center for Biomedical Information in the Institute for Computational Biomedicine at Weill Cornell Medical College.

References:

1 Wacker, D., Stevens, R. C. & Roth, B. L. How Ligands Illuminate GPCR Molecular Pharmacology. *Cell* **170**, 414-427, doi:10.1016/j.cell.2017.07.009 (2017).

2 Sriram, K. & Insel, P. A. G Protein-Coupled Receptors as Targets for Approved Drugs: How Many Targets and How Many Drugs? *Mol Pharmacol* **93**, 251-258, doi:10.1124/mol.117.111062 (2018).

3 Maeda, S., Qu, Q., Robertson, M. J., Skiniotis, G. & Kobilka, B. K. Structures of the M1 and M2 muscarinic acetylcholine receptor/G-protein complexes. *Science* **364**, 552-557, doi:10.1126/science.aaw5188 (2019).

4 Tsai, C. J. *et al.* Cryo-EM structure of the rhodopsin-Galphai-betagamma complex reveals binding of the rhodopsin C-terminal tail to the gbeta subunit. *Elife* **8**, doi:10.7554/eLife.46041 (2019).

5 Seven, A. B. *et al.* G-protein activation by a metabotropic glutamate receptor. *Nature* **595**, 450-454, doi:10.1038/s41586-021-03680-3 (2021).

6 Kisselev, O. G., McDowell, J. H. & Hargrave, P. A. The arrestin-bound conformation and dynamics of the phosphorylated carboxy-terminal region of rhodopsin. *FEBS Lett* **564**, 307-311, doi:10.1016/S0014-5793(04)00226-1 (2004).

7 Shukla, A. K. *et al.* Structure of active beta-arrestin-1 bound to a G-protein-coupled receptor phosphopeptide. *Nature* **497**, 137-141, doi:10.1038/nature12120 (2013).

8 Min, K. *et al.* Crystal Structure of beta-Arrestin 2 in Complex with CXCR7 Phosphopeptide. *Structure* **28**, 1014-1023 e1014, doi:10.1016/j.str.2020.06.002 (2020).

9 Zhou, X. E. *et al.* Identification of Phosphorylation Codes for Arrestin Recruitment by G Protein-Coupled Receptors. *Cell* **170**, 457-469 e413, doi:10.1016/j.cell.2017.07.002 (2017).

10 Yin, W. *et al.* A complex structure of arrestin-2 bound to a G protein-coupled receptor. *Cell Res* **29**, 971-983, doi:10.1038/s41422-019-0256-2 (2019).

11 Staus, D. P. *et al.* Structure of the M2 muscarinic receptor-beta-arrestin complex in a lipid nanodisc. *Nature* **579**, 297-302, doi:10.1038/s41586-020-1954-0 (2020).

12 Huang, W. *et al.* Structure of the neurotensin receptor 1 in complex with beta-arrestin 1. *Nature* **579**, 303-308, doi:10.1038/s41586-020-1953-1 (2020).

13 Guillien, M. *et al.* Structural Insights into the Intrinsically Disordered GPCR C-Terminal Region, Major Actor in Arrestin-GPCR Interaction. *Biomolecules* **12**, doi:10.3390/biom12050617 (2022).

bioRxiv preprint doi: https://doi.org/10.1101/2023.08.16.553551; this version posted August 17, 2023. The copyright holder for this preprint (which was not certified by peer review) is the author/funder, who has granted bioRxiv a license to display the preprint in perpetuity. It is made available under aCC-BY-NC-ND 4.0 International license.

14 Guillien, M. *et al.* Phosphorylation motif dictates GPCR C-terminal domain conformation and arrestin interaction. *bioRxiv*, 2023.2002.2023.529712, doi:10.1101/2023.02.23.529712 (2023).

15 Heng, J. *et al.* Function and dynamics of the intrinsically disordered carboxyl terminus of beta2 adrenergic receptor. *Nat Commun* **14**, 2005, doi:10.1038/s41467-023-37233-1 (2023).

16 Shiraishi, Y. *et al.* Phosphorylation-induced conformation of beta(2)-adrenoceptor related to arrestin recruitment revealed by NMR. *Nat Commun* **9**, 194, doi:10.1038/s41467-017-02632-8 (2018).

17 Ahn, K. H. *et al.* Structural analysis of the human cannabinoid receptor one carboxyl-terminus identifies two amphipathic helices. *Biopolymers* **91**, 565-573, doi:10.1002/bip.21179 (2009).

18 Patwardhan, A., Cheng, N. & Trejo, J. Post-Translational Modifications of G Protein-Coupled Receptors Control Cellular Signaling Dynamics in Space and Time. *Pharmacol Rev* **73**, 120-151, doi:10.1124/pharmrev.120.000082 (2021).

19 Song, W., Yen, H. Y., Robinson, C. V. & Sansom, M. S. P. State-dependent Lipid Interactions with the A2a Receptor Revealed by MD Simulations Using In Vivo-Mimetic Membranes. *Structure* **27**, 392-403 e393, doi:10.1016/j.str.2018.10.024 (2019).

20 Dawaliby, R. *et al.* Allosteric regulation of G protein-coupled receptor activity by phospholipids. *Nat Chem Biol* **12**, 35-39, doi:10.1038/nchembio.1960 (2016).

21 Yen, H. Y. *et al.* PtdIns(4,5)P2 stabilizes active states of GPCRs and enhances selectivity of G-protein coupling. *Nature* **559**, 423-427, doi:10.1038/s41586-018-0325-6 (2018).

22 Janetzko, J. *et al.* Membrane phosphoinositides regulate GPCR-beta-arrestin complex assembly and dynamics. *Cell* **185**, 4560-4573 e4519, doi:10.1016/j.cell.2022.10.018 (2022).

23 Grimes, J. *et al.* Single-molecule analysis of receptor-β-arrestin interactions in living cells. *bioRxiv*, 2022.2011.2015.516577, doi:10.1101/2022.11.15.516577 (2022).

24 Chen, Q. *et al.* ACKR3-arrestin2/3 complexes reveal molecular consequences of GRK-dependent barcoding. *bioRxiv*, doi:10.1101/2023.07.18.549504 (2023).

25 Ellaithy, A., Gonzalez-Maeso, J., Logothetis, D. A. & Levitz, J. Structural and Biophysical Mechanisms of Class C G Protein-Coupled Receptor Function. *Trends Biochem Sci* **45**, 1049-1064, doi:10.1016/j.tibs.2020.07.008 (2020).

26 Dore, A. S. *et al.* Structure of class C GPCR metabotropic glutamate receptor 5 transmembrane domain. *Nature* **511**, 557-562, doi:10.1038/nature13396 (2014).

27 Wu, H. *et al.* Structure of a class C GPCR metabotropic glutamate receptor 1 bound to an allosteric modulator. *Science* **344**, 58-64, doi:10.1126/science.1249489 (2014).

28 Du, J. *et al.* Structures of human mGlu2 and mGlu7 homo- and heterodimers. *Nature* **594**, 589-593, doi:10.1038/s41586-021-03641-w (2021).

29 Enz, R. Structure of metabotropic glutamate receptor C-terminal domains in contact with interacting proteins. *Front Mol Neurosci* **5**, 52, doi:10.3389/fnmol.2012.00052 (2012).

30 Reiner, A. & Levitz, J. Glutamatergic Signaling in the Central Nervous System: Ionotropic and Metabotropic Receptors in Concert. *Neuron* **98**, 1080-1098, doi:10.1016/j.neuron.2018.05.018 (2018).

bioRxiv preprint doi: https://doi.org/10.1101/2023.08.16.553551; this version posted August 17, 2023. The copyright holder for this preprint (which was not certified by peer review) is the author/funder, who has granted bioRxiv a license to display the preprint in perpetuity. It is made available under aCC-BY-NC-ND 4.0 International license.

31 Pin, J. P. & Bettler, B. Organization and functions of mGlu and GABA(B) receptor complexes. *Nature* **540**, 60-68, doi:10.1038/nature20566 (2016).
32 Suh, Y. H., Chang, K. & Roche, K. W. Metabotropic glutamate receptor trafficking. *Mol Cell Neurosci* **91**, 10-24, doi:10.1016/j.mcn.2018.03.014 (2018).
33 Abreu, N., Acosta-Ruiz, A., Xiang, G. & Levitz, J. Mechanisms of differential desensitization of metabotropic glutamate receptors. *Cell Rep* **35**, 109050, doi:10.1016/j.celrep.2021.109050 (2021).
34 Lin, S. *et al.* Structures of G(i)-bound metabotropic glutamate receptors mGlu2 and mGlu4. *Nature* **594**, 583-588, doi:10.1038/s41586-021-03495-2 (2021).
35 Koehl, A. *et al.* Structural insights into the activation of metabotropic glutamate receptors. *Nature* **566**, 79-84, doi:10.1038/s41586-019-0881-4 (2019).
36 Nasrallah, C. *et al.* Agonists and allosteric modulators promote signaling from different metabotropic glutamate receptor 5 conformations. *Cell Rep* **36**, 109648, doi:10.1016/j.celrep.2021.109648 (2021).
37 Das, T. & Eliezer, D. Membrane interactions of intrinsically disordered proteins: The example of alpha-synuclein. *Biochim Biophys Acta Proteins Proteom* **1867**, 879-889, doi:10.1016/j.bbapap.2019.05.001 (2019).
38 Das, T. & Eliezer, D. Probing Structural Changes in Alpha-Synuclein by Nuclear Magnetic Resonance Spectroscopy. *Methods Mol Biol* **1948**, 157-181, doi:10.1007/978-1-4939-9124-2_13 (2019).
39 Snead, D. & Eliezer, D. Spectroscopic Characterization of Structure-Function Relationships in the Intrinsically Disordered Protein Complexin. *Methods Enzymol* **611**, 227-286, doi:10.1016/bs.mie.2018.08.005 (2018).
40 Parker, W. & Song, P. S. Protein structures in SDS micelle-protein complexes. *Biophys J* **61**, 1435-1439, doi:10.1016/S0006-3495(92)81949-5 (1992).
41 Bussell, R., Jr. & Eliezer, D. A structural and functional role for 11-mer repeats in alpha-synuclein and other exchangeable lipid binding proteins. *J Mol Biol* **329**, 763-778 (2003).
42 Snead, D. *et al.* Unique Structural Features of Membrane-Bound C-Terminal Domain Motifs Modulate Complexin Inhibitory Function. *Front Mol Neurosci* **10**, 154, doi:10.3389/fnmol.2017.00154 (2017).
43 Dijkman, P. M. *et al.* Conformational dynamics of a G protein-coupled receptor helix 8 in lipid membranes. *Sci Adv* **6**, eaav8207, doi:10.1126/sciadv.aav8207 (2020).
44 McDonald, S. K. & Fleming, K. G. Aromatic Side Chain Water-to-Lipid Transfer Free Energies Show a Depth Dependence across the Membrane Normal. *J Am Chem Soc* **138**, 7946-7950, doi:10.1021/jacs.6b03460 (2016).
45 Moon, C. P. & Fleming, K. G. Side-chain hydrophobicity scale derived from transmembrane protein folding into lipid bilayers. *Proc Natl Acad Sci U S A* **108**, 10174-10177, doi:10.1073/pnas.1103979108 (2011).
46 Killian, J. A. & von Heijne, G. How proteins adapt to a membrane-water interface. *Trends Biochem Sci* **25**, 429-434, doi:10.1016/s0968-0004(00)01626-1 (2000).
47 Prickett, T. D. *et al.* Exon capture analysis of G protein-coupled receptors identifies activating mutations in GRM3 in melanoma. *Nat Genet* **43**, 1119-1126, doi:10.1038/ng.950 (2011).

bioRxiv preprint doi: https://doi.org/10.1101/2023.08.16.553551; this version posted August 17, 2023. The copyright holder for this preprint (which was not certified by peer review) is the author/funder, who has granted bioRxiv a license to display the preprint in perpetuity. It is made available under aCC-BY-NC-ND 4.0 International license.

48 Asher, W. B. *et al.* GPCR-mediated beta-arrestin activation deconvoluted with single-molecule precision. *Cell* **185**, 1661-1675 e1616, doi:10.1016/j.cell.2022.03.042 (2022).

49 Xu, C. *et al.* Regulation of T cell receptor activation by dynamic membrane binding of the CD3epsilon cytoplasmic tyrosine-based motif. *Cell* **135**, 702-713, doi:10.1016/j.cell.2008.09.044 (2008).

50 Wang, Y. *et al.* Regulation of EGFR nanocluster formation by ionic protein-lipid interaction. *Cell Res* **24**, 959-976, doi:10.1038/cr.2014.89 (2014).

51 Cornish, J., Chamberlain, S. G., Owen, D. & Mott, H. R. Intrinsically disordered proteins and membranes: a marriage of convenience for cell signalling? *Biochem Soc Trans* **48**, 2669-2689, doi:10.1042/BST20200467 (2020).

52 Fang, W. *et al.* Structural basis of the activation of metabotropic glutamate receptor 3. *Cell Res* **32**, 695-698, doi:10.1038/s41422-022-00623-z (2022).

53 Morton, L. A. *et al.* MARCKS-ED peptide as a curvature and lipid sensor. *ACS Chem Biol* **8**, 218-225, doi:10.1021/cb300429e (2013).

54 Wang, J. *et al.* Lateral sequestration of phosphatidylinositol 4,5-bisphosphate by the basic effector domain of myristoylated alanine-rich C kinase substrate is due to nonspecific electrostatic interactions. *J Biol Chem* **277**, 34401-34412, doi:10.1074/jbc.M203954200 (2002).

55 Snead, D., Wragg, R. T., Dittman, J. S. & Eliezer, D. Membrane curvature sensing by the C-terminal domain of complexin. *Nat Commun* **5**, 4955, doi:10.1038/ncomms5955 (2014).

56 Wragg, R. T. *et al.* Evolutionary Divergence of the C-terminal Domain of Complexin Accounts for Functional Disparities between Vertebrate and Invertebrate Complexins. *Front Mol Neurosci* **10**, 146, doi:10.3389/fnmol.2017.00146 (2017).

57 Hicks, A., Escobar, C. A., Cross, T. A. & Zhou, H. X. Fuzzy Association of an Intrinsically Disordered Protein with Acidic Membranes. *JACS Au* **1**, 66-78, doi:10.1021/jacsau.0c00039 (2021).

58 Dikiy, I. *et al.* Semisynthetic and in Vitro Phosphorylation of Alpha-Synuclein at Y39 Promotes Functional Partly Helical Membrane-Bound States Resembling Those Induced by PD Mutations. *ACS Chem Biol* **11**, 2428-2437, doi:10.1021/acschembio.6b00539 (2016).

59 Acosta, D. M., Mancinelli, C., Bracken, C. & Eliezer, D. Post-translational modifications within tau paired helical filament nucleating motifs perturb microtubule interactions and oligomer formation. *J Biol Chem* **298**, 101442, doi:10.1016/j.jbc.2021.101442 (2022).

60 Tobin, A. B. G-protein-coupled receptor phosphorylation: where, when and by whom. *Br J Pharmacol* **153 Suppl 1**, S167-176, doi:10.1038/sj.bjp.0707662 (2008).

61 Nobles, K. N. *et al.* Distinct phosphorylation sites on the beta(2)-adrenergic receptor establish a barcode that encodes differential functions of beta-arrestin. *Sci Signal* **4**, ra51, doi:10.1126/scisignal.2001707 (2011).

62 Gao, Y. *et al.* Asymmetric activation of the calcium-sensing receptor homodimer. *Nature* **595**, 455-459, doi:10.1038/s41586-021-03691-0 (2021).

bioRxiv preprint doi: https://doi.org/10.1101/2023.08.16.553551; this version posted August 17, 2023. The copyright holder for this preprint (which was not certified by peer review) is the author/funder, who has granted bioRxiv a license to display the preprint in perpetuity. It is made available under aCC-BY-NC-ND 4.0 International license.

63 Pluhackova, K., Wilhelm, F. M. & Muller, D. J. Lipids and Phosphorylation Conjointly Modulate Complex Formation of beta(2)-Adrenergic Receptor and beta-arrestin2. *Front Cell Dev Biol* **9**, 807913, doi:10.3389/fcell.2021.807913 (2021).

64 Wang, X. *et al.* Structural insights into dimerization and activation of the mGlu2-mGlu3 and mGlu2-mGlu4 heterodimers. *Cell Res*, doi:10.1038/s41422-023-00830-2 (2023).

65 Kjaergaard, M. & Poulsen, F. M. Sequence correction of random coil chemical shifts: correlation between neighbor correction factors and changes in the Ramachandran distribution. *J Biomol NMR* **50**, 157-165, doi:10.1007/s10858-011-9508-2 (2011).

66 Kjaergaard, M., Brander, S. & Poulsen, F. M. Random coil chemical shift for intrinsically disordered proteins: effects of temperature and pH. *J Biomol NMR* **49**, 139-149, doi:10.1007/s10858-011-9472-x (2011).

67 Jumper, J. *et al.* Highly accurate protein structure prediction with AlphaFold. *Nature* **596**, 583-589, doi:10.1038/s41586-021-03819-2 (2021).

68 Mirdita, M. *et al.* ColabFold: making protein folding accessible to all. *Nat Methods* **19**, 679-682, doi:10.1038/s41592-022-01488-1 (2022).

69 Jo, S., Kim, T., Iyer, V. G. & Im, W. CHARMM-GUI: a web-based graphical user interface for CHARMM. *J Comput Chem* **29**, 1859-1865, doi:10.1002/jcc.20945 (2008).

70 Brooks, B. R. *et al.* CHARMM: the biomolecular simulation program. *J Comput Chem* **30**, 1545-1614, doi:10.1002/jcc.21287 (2009).

71 Lee, J. *et al.* CHARMM-GUI Input Generator for NAMD, GROMACS, AMBER, OpenMM, and CHARMM/OpenMM Simulations Using the CHARMM36 Additive Force Field. *J Chem Theory Comput* **12**, 405-413, doi:10.1021/acs.jctc.5b00935 (2016).

72 Wu, E. L. *et al.* CHARMM-GUI Membrane Builder toward realistic biological membrane simulations. *J Comput Chem* **35**, 1997-2004, doi:10.1002/jcc.23702 (2014).

73 Jo, S., Lim, J. B., Klauda, J. B. & Im, W. CHARMM-GUI Membrane Builder for mixed bilayers and its application to yeast membranes. *Biophys J* **97**, 50-58, doi:10.1016/j.bpj.2009.04.013 (2009).

74 Jo, S., Kim, T. & Im, W. Automated builder and database of protein/membrane complexes for molecular dynamics simulations. *PLoS One* **2**, e880, doi:10.1371/journal.pone.0000880 (2007).

75 Lee, J. *et al.* CHARMM-GUI Membrane Builder for Complex Biological Membrane Simulations with Glycolipids and Lipoglycans. *J Chem Theory Comput* **15**, 775-786, doi:10.1021/acs.jctc.8b01066 (2019).

76 Eastman, P. *et al.* OpenMM 7: Rapid development of high performance algorithms for molecular dynamics. *PLoS Comput Biol* **13**, e1005659, doi:10.1371/journal.pcbi.1005659 (2017).

77 Huang, J. *et al.* CHARMM36m: an improved force field for folded and intrinsically disordered proteins. *Nat Methods* **14**, 71-73, doi:10.1038/nmeth.4067 (2017).

78 Humphrey, W., Dalke, A. & Schulten, K. VMD: visual molecular dynamics. *J Mol Graph* **14**, 33-38, 27-38, doi:10.1016/0263-7855(96)00018-5 (1996).

79 Marx, D. C. & Fleming, K. G. Local Bilayer Hydrophobicity Modulates Membrane Protein Stability. *J Am Chem Soc* **143**, 764-772, doi:10.1021/jacs.0c09412 (2021).

bioRxiv preprint doi: https://doi.org/10.1101/2023.08.16.553551; this version posted August 17, 2023. The copyright holder for this preprint (which was not certified by peer review) is the author/funder, who has granted bioRxiv a license to display the preprint in perpetuity. It is made available under aCC-BY-NC-ND 4.0 International license.

80 Fleming, P. J. & Fleming, K. G. HullRad: Fast Calculations of Folded and Disordered Protein and Nucleic Acid Hydrodynamic Properties. *Biophys J* **114**, 856-869, doi:10.1016/j.bpj.2018.01.002 (2018).

81 Fleming, P. J., Correia, J. J. & Fleming, K. G. Revisiting macromolecular hydration with HullRadSAS. *Eur Biophys J*, doi:10.1007/s00249-022-01627-8 (2023).

82 Gutzeit, V. A. *et al.* A fine-tuned azobenzene for enhanced photopharmacology in vivo. *Cell Chem Biol* **28**, 1648-1663 e1616, doi:10.1016/j.chembiol.2021.02.020 (2021).

83 Vivaudou, M. *et al.* Probing the G-protein regulation of GIRK1 and GIRK4, the two subunits of the KACh channel, using functional homomeric mutants. *J Biol Chem* **272**, 31553-31560, doi:10.1074/jbc.272.50.31553 (1997).

bioRxiv preprint doi: https://doi.org/10.1101/2023.08.16.553551; this version posted August 17, 2023. The copyright holder for this preprint (which was not certified by peer review) is the author/funder, who has granted bioRxiv a license to display the preprint in perpetuity. It is made available under aCC-BY-NC-ND 4.0 International license.

Figure Legends:

Figure 1: An NMR-based assay reveals phospholipid membrane binding of the intrinsically disordered mGluR2 and mGluR3 CTDs. (A) Schematic of the structural organization of mGluR domains highlighting the location of the CTD compared to the ordered parts of the protein and the membrane. **(B)** Schematic of NMR-based CTD-membrane binding assay that takes advantage of changes in tumbling rates of the CTD due to interactions with LUVs. **(C)** ^{1}H-^{15}N HSQC spectra of isolated mGluR2* and **(D)** mGluR3* CTD in the presence (red) and absence (black) of 10 mM 100 nm diameter LUVs comprised of DOPS at pH 6.8 at 10 °C, with zoomed insets of crowded regions, highlighting loss of signal of specific residues in the presence of LUVs.

Figure 2: N-terminal regions of mGluR2 and 3 CTDs interact with negatively charged lipids. NMR intensity ratios for **(A)** mGluR2 and **(B)** mGluR3 from spectra collected with and without LUVs of three different lipid compositions. Prolines, which do not give rise to signals in ^{1}H-^{15}N HSQC spectra, are denoted by *, overlapping peaks for which values were not included by **, and residues not detected in the spectra by ***. **(C)** Averaged intensity ratios over the first ~20 residues (mGluR2 Q822-A842; mGluR3 Q831-T851) illustrate the lipid composition dependence of the interactions in this region (±s.e.m.). **(D)** Averaged intensity ratios over the last ~20 residues (mGluR2 Q853-L872; mGluR3 Y861-L879) illustrate the lack of lipid composition dependence of the interactions in this region (±s.e.m.).

Figure 3: An N-terminal cluster of basic residues is critical for CTD membrane binding. (A) sequence alignment of the first 15 residues of the mGluR2 and mGluR3 CTDs highlighting conserved (*) and positively charged (highlighted) residues. **(B)** Intensity ratio plots of mGluR2 CTD constructs containing alanine substitutions for each of the four basic residues from spectra collected with and without LUVs containing a 1:1 mixture of DOPS:DOPC lipids. **(C)** Averaged intensity ratios over the first ~20 residues (Q822-A842) illustrate the regional effect of each mutation for LUVs of different lipid composition (±s.e.m.). **(D)** Averaged intensity ratios over the last ~20 residues (Q853-L872) illustrate the regional effect of each mutation for LUVs of different lipid composition (±s.e.m.).

Figure 4: Molecular dynamics simulations reveal multi-modal membrane interactions of the intrinsically disordered mGluR3-CTD. (A) Snapshots of mGluR3 TM7-CTD replica 6 trajectory, highlighting three conformations of the CTD: the beginning of the simulation with no membrane contacts (t=0, left), a highly extended membrane-binding mode (t=174.4 ns, middle), and a partially extended binding (t=224 ns, right) **(B)** Comparison of the intensity ratios for the mGluR3 CTD in the presence of 1:1 DOPS:DOPC LUVs (blue, right axis) with the average distance of each residue from the lipid phosphate plane over the course of the simulation (black, left axis). **(C)** Interactions between CTD residue side chains and lipids: Left, black – total number of hydrogen bonds between each side chain and lipid headgroups; Right, red – average percent buried surface area of each side chain in the membrane.

Figure 5: Membrane interactions of the S/T-rich region of the mGluR3 CTD is modulated by mutation of a key residue and by cancer mutations. (A) mGluR3-CTD sequence annotated with the NMR- and MD-determined membrane binding region and the overlapping Ser/Thr-rich region (* denotes residues conserved in mGluR2). **(B)** Snapshots of residue Y853 (shown as slate blue spheres) in membrane-embedded and membrane-associated positions (from MD replica 6). Lipid phosphates are shown as transparent orange spheres and lipid chains in contact with Y853 are shown in stick representation (DOPS in magenta and DOPC in salmon). Remaining lipids are shown in transparent gray and the protein backbone is shown in gray in cartoon representation. **(C)** Percent buried surface area of Y853 in the lipid bilayer plotted as a function of time in MD replica 6. **(D)** Comparison of the averaged integrated NMR intensity ratios of WT mGluR3-CTD (dotted blue) with Y853A mGluR3-CTD taken over the S/T-rich region (S845-T860) as a function of LUV lipid composition (±s.e.m.; Wilcoxon test; *$p<0.05$, ***$p<0.001$, n.s. $p\geq0.05$). **(E)** Snapshots of residues R843 (blue), G848 (orange) and E870 (red) at different time points during the time course of MD replica 6 showing prolonged membrane-association of R843 and G848 and fluctuating membrane-association of E870 (side chains shown as spheres colored as in **(F)** below; otherwise rendered and colored as above in **(B)**). **(F)** Position of side chains R843, G848, and E870 relative to the phosphate plane of the membrane (see methods) throughout the time course of MD replica 6. **(G)**

bioRxiv preprint doi: https://doi.org/10.1101/2023.08.16.553551; this version posted August 17, 2023. The copyright holder for this preprint (which was not certified by peer review) is the author/funder, who has granted bioRxiv a license to display the preprint in perpetuity. It is made available under aCC-BY-NC-ND 4.0 International license.

Comparison of the averaged NMR intensity ratios of WT mGluR3-CTD (dotted blue) with melanoma-associated mutations G848E mGluR3-CTD (orange) taken over the S/T-rich region (S845-T860) as a function of LUV lipid composition (±s.e.m.; Wilcoxon test; **p<0.01, ***p<0.001). **(H)** and E870K mGluR3-CTD (red) taken over the last 19 residues (Y861-L879) as a function of LUV lipid composition (±s.e.m.; Wilcoxon test; ***p<0.001).

Figure 6: CTD mutations that alter membrane binding affect mGluR3 internalization and function. **(A)** Schematics of mGluR3 CTD mutational positions and their effects on mGluR3-CTD free vs. membrane bound equilibrium. Larger arrows show the direction in which each variant perturbs the equilibrium. **(B)** Quantification of the extent of receptor internalization for each mGluR3 variant (with dotted line denoting mGluR3 WT internalization) (averaged internalization per day, 10-12 images per condition/day and 4-9 days per condition; One-Way ANOVA with multiple comparisons, * p<0.05 *** p<0.001). **(C)** Representative images of HEK 293T cells expressing SNAP-tagged mGluR3 variants incubated for 30 min with 1 mM Glu (red arrows represent internalized receptors; scale bar: 5 μm). **(D)** Glutamate dose response curves for mGluR3 variants in a patch-clamp experiment using GIRK currents as a reporter for mGluR3 G-protein activation (EC50: WT = 136.9 ± 26.9 nM, G848E = 44.2 ± 8.6 nM, Y853A = 417.8 ± 64.8 nM, E870K = 101.6 ± 21.7 nM, CAAX = 156.9 ± 42.8 nM; F-test of EC50 shifts; **p<0.01, ***p<0.001). **(E)** Quantification of the extent of recepor internalization of WT mGluR3 vs. Y853D phospho-mimetic mutant (averaged internalization of 10 images per condition/day across 3 days; t-test; *p<0.05. **(F)** Representative images of HEK293T cells expressing SNAP-tagged mGluR3 WT vs Y853A treated with 100 ng/ml EGF for 30 min (red arrows represent internalization; scale bar: 5 μm). **(G)** Quantification of the extent of internalization for mGluR3 WT vs Y853A mutant in EGF or Glu+EGF incubated conditions (averaged internalization per day, 10 images condition/day and 3-4 days per condition; t-test, **p<0.01 , n.s. p≥0.05). **(H)** Working model of mGluR3-CTD free vs. membrane bound equilibrium and changes that favor the less accessible membrane-bound (E870K, anionic lipids) or the more accessible free (Y853A, G848E, phosphorylation) state.

Figure S1: NMR spectra of mGluR2 and mGluR3 with LUVs of different compositions and of WT and cysteine-free variants. ^{1}H-^{15}N HSQC spectra of mGluR2 **(A,B)** and mGluR3 **(D,E)** CTDs in the presence (purple or light blue) and absence (black) of LUVs comprised of 1:1 DOPS:DOPC **(A,D)** or DOPC **(B,E)** with zoomed insets of crowded regions highlighting loss of signal of specific residues in the presence of LUVs. ^{1}H-^{15}N HSQC spectra of **(C)** mGluR2 WT (dark blue) and WT* (C859A mutant, red) CTD and **(F)** mGluR3 WT (dark blue) and WT* (C866A mutant, red) CTD. Chemical shift changes are confined to residues in the immediate vicinity of the mutations.

Figure S2: Secondary structure analysis of mGluR CTDs using CD. Circular dichroism spectra of the mGluR2 **(A)** and mGluR3 **(B)** CTD and mGluR2 **(C)** and mGluR3 **(D)** peptides encompassing the NMR determined binding region (first 23 residues) in the absence of LUVs (black) or in the presence of 10 mM, 100 nm diameter **(A)** or 50 nm diameter **(B-D)** DOPC (blue), 1:1 DOPS:DOPC (purple) or DOPS (red) LUVs under conditions where NMR indicates no (DOPC) or complete (DOPS or 1:1 DOPS:DOPC) CTD binding. Note that for **(A)** the sudden increase in signal below 205 nm results from increased scattering due to the use of 100 nm diameter LUVs in these samples. For **(D)** the spectra suggest a degree of β-strand formation, possibly due to intermolecular interactions caused by the limited solubility of this peptide **(E)** CD spectra of mGluR3 peptides encompassing the NMR determined binding region (first 23 residues) in the absence (black) or presence of 40 mM SDS (red) or 71 mM DPC (blue). **(F)** CD spectra of NTSR1 peptide free in solution (black) and in the presence of 10 mM 50 nm diameter DOPS LUVs (red). **(G,H)** Helical wheel representations of the first 20 residues of the mGluR2 **(G)** and mGluR3 **(H)** CTD illustrating the lack of clear amphipathic character (basic residue in blue, polar residues in yellow, apolar residues in white).

Figure S3: Secondary structure analysis of mGluR CTDs using NMR. Secondary C_α chemical shifts for the mGluR2 **(A)** and mGluR3 **(B)** CTDs free in solution. Positive/negative deviations greater than 1.0 PPM indicate a propensity for helical/β-strand secondary structure, respectively.

bioRxiv preprint doi: https://doi.org/10.1101/2023.08.16.553551; this version posted August 17, 2023. The copyright holder for this preprint (which was not certified by peer review) is the author/funder, who has granted bioRxiv a license to display the preprint in perpetuity. It is made available under aCC-BY-NC-ND 4.0 International license.

Figure S4: Mutating positively charged residues impacts CTD-membrane interactions. ^{1}H-^{15}N HSQC spectra of mGluR2 CTD variants in the presence (purple) and absence (black) of 100 nm LUVs comprised of 1:1 DOPS:DOPC.

Figure S5: mGluR CTDs LUVs binding as a function of vesicle size. (A) NMR intensity ratio plots for the mGluR2-CTD in the presence of DOPS LUVs of varying diameter. **(B)** Averaged intensity ratios over the first ~20 residues (Q822-A842) (±s.e.m.). **(C)** Averaged intensity ratios over the last ~20 residues (Q853-L872) (±s.e.m.).

Figure S6: Lipid titration identifies weaker and stronger interaction regions of the mGluR3 CTD. (A) NMR intensity ratios for the mGluR3-CTD in the presence of varying concentrations of 1:1 DOPS:DOPC LUVs. **(B)** Average intensity ratios over different regions of the mGluR3 CTD highlight the greater sensitivity of the S/T-rich region to lipid concentration (±s.e.m.).

Figure S7: MD simulations capture mGluR3 CTD-membrane interactions and confirm absence of regular secondary structure. (**A-F)** (i, left) snapshots of starting and ending frames of each MD simulation replica of the mGluR3 TM7-CTD construct with the protein shown in black cartoon representation and lipid phosphates as orange spheres; (ii, middle) average residue distance from the phosphate plane in each replica with error bars corresponding to standard deviations; (iii, right) Percent of trajectory frames for each CTD residue residing in disordered (black), helical (red), or beta-sheet (blue) secondary structure during each replica trajectory.

Figure S8: Comparison and analysis of MD simulation replicas. (A) Radius of gyration for the CTD (residues 830-879) during the course of each MD replica. **(B)** Violin plots of radii of gyration for each MD replica annotated with mean (thick dotted line) and one standard deviation (thin dotted lines). **(C)** Comparison of the intensity ratios for the mGluR3 CTD in the presence of 2.5 mM 1:1 DOPS:DOPC LUVs (blue, right axis) with the average distance of each residue from the lipid phosphate plane over the course of the MD replica 5 (black, left axis). Note that the discrepancy at the very N-terminus may arise from the CTD being membrane-anchored in the simulations but not in the NMR experiments. **(D)** Total number of hydrogen bonds between side chains of each CTD residue and DOPS lipid headgroups from MD replica 5. **(E, F)** Position of arginine side chains relative to the phosphate plane of the membrane (see methods) throughout the time course of MD replica 5 **(E)** and 6 **(F)**. **(G)** Total number of hydrogen bonds summed from MD replicas 5 and 6 between each arginine side chain and DOPC or DOPS lipid headgroups, highlighting the preference for interactions with negatively charged PS headgroups.

Figure S9: Y853 and cancer-associated mutations modulate membrane binding of the mGlur3 S/T-rich region. (A) Distance from phosphate plane of side chains in the S/T-rich region as a function of time for Y853 and nearby S/T residues in MD replica 6. **(B)** Snapshots of S/T residues in the S/T-rich region position relative to the membrane highlighting the dynamics of the region during our simulations. Side chains are shown as spheres (Ser in green and Thr in blue) and lipid phosphates are shown as orange spheres. Protein backbone is in gray cartoon **(C)** ^{1}H-^{15}N HSQC spectra of mGluR3 CTD variants in the presence (purple) and absence (black) of 1:1 DOPS:DOPC. **(D)** NMR intensity ratios WT (dotted blue line), Y853A (purple), G848E (orange), and E870K (red) mGluR3-CTD in the presence of 10 mM 100 nm diameter LUVs comprised of 1:1 DOPS:DOPC 100 nm LUVs.

Figure S10: Surface expression of CTD-mutants and functional effects of G848E on mGluR3 activity. (A) Surface expression quantification for all the mutants tested in the study (One-way ANOVA with multiple comparisons; * $p<0.05$, *** $p<0.001$. **(B-C)** Representative traces of evoked GIRK potassium currents after mGluR3 activation by different doses of glutamate (10 nM, 100 nM and 10 μM) in WT **(B)** and G848E mutant **(C).**

bioRxiv preprint doi: https://doi.org/10.1101/2023.08.16.553551; this version posted August 17, 2023. The copyright holder for this preprint (which was not certified by peer review) is the author/funder, who has granted bioRxiv a license to display the preprint in perpetuity. It is made available under aCC-BY-NC-ND 4.0 International license.

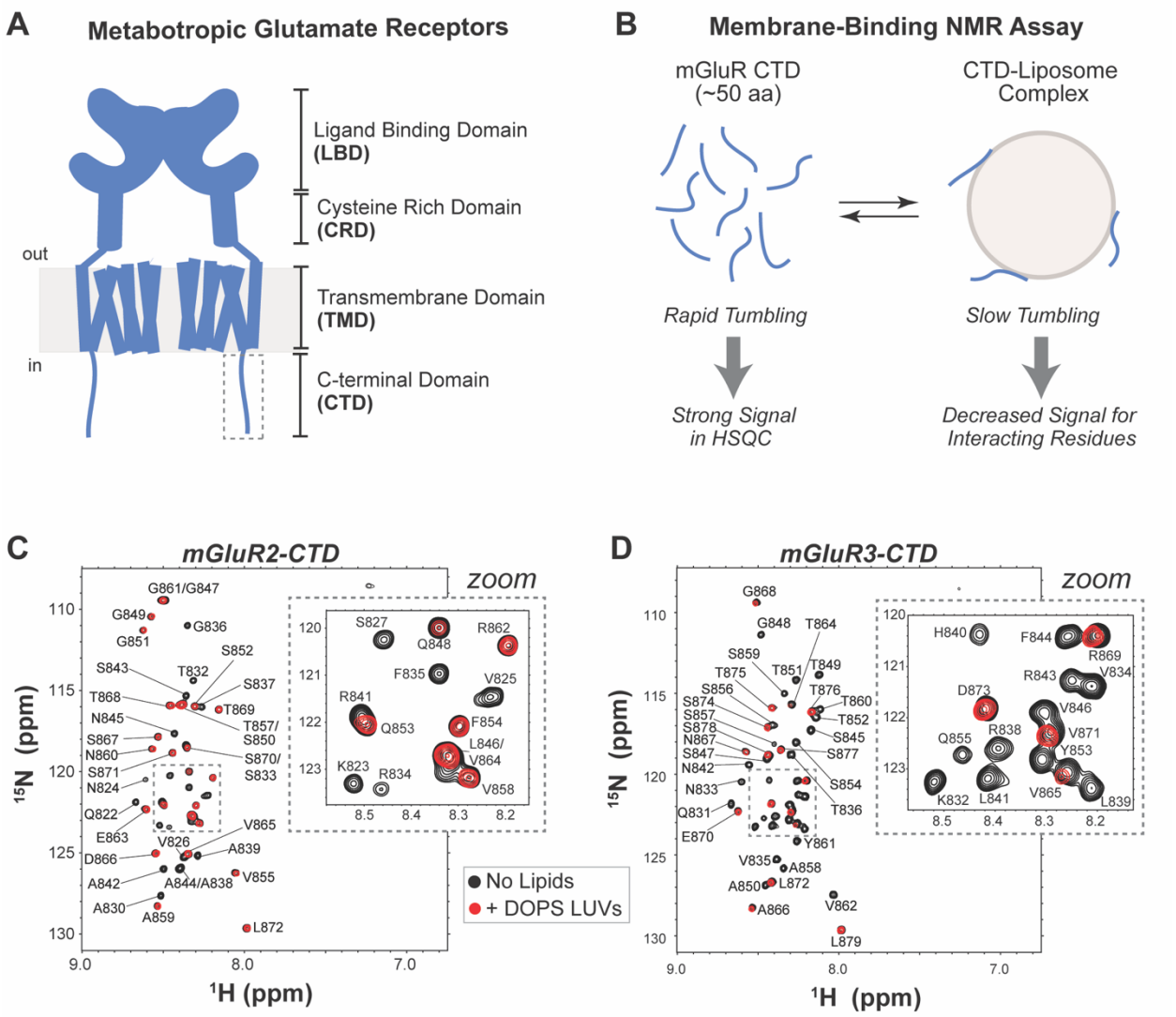

Figure 1: An NMR-based assay reveals phospholipid membrane binding of the intrinsically disordered mGluR2 and mGluR3 CTDs. **(A)** Schematic of the structural organization of mGluR domains highlighting the location of the CTD compared to the ordered parts of the protein and the membrane. **(B)** Schematic of NMR-based CTD-membrane binding assay that takes advantage of changes in tumbling rates of the CTD due to interactions with LUVs. **(C)** ^{1}H-^{15}N HSQC spectra of isolated mGluR2* and **(D)** mGluR3* CTD in the presence (red) and absence (black) of 10 mM 100 nm diameter LUVs comprised of DOPS at pH 6.8 at 10 °C, with zoomed insets of crowded regions, highlighting loss of signal of specific residues in the presence of LUVs.

bioRxiv preprint doi: https://doi.org/10.1101/2023.08.16.553551; this version posted August 17, 2023. The copyright holder for this preprint (which was not certified by peer review) is the author/funder, who has granted bioRxiv a license to display the preprint in perpetuity. It is made available under aCC-BY-NC-ND 4.0 International license.

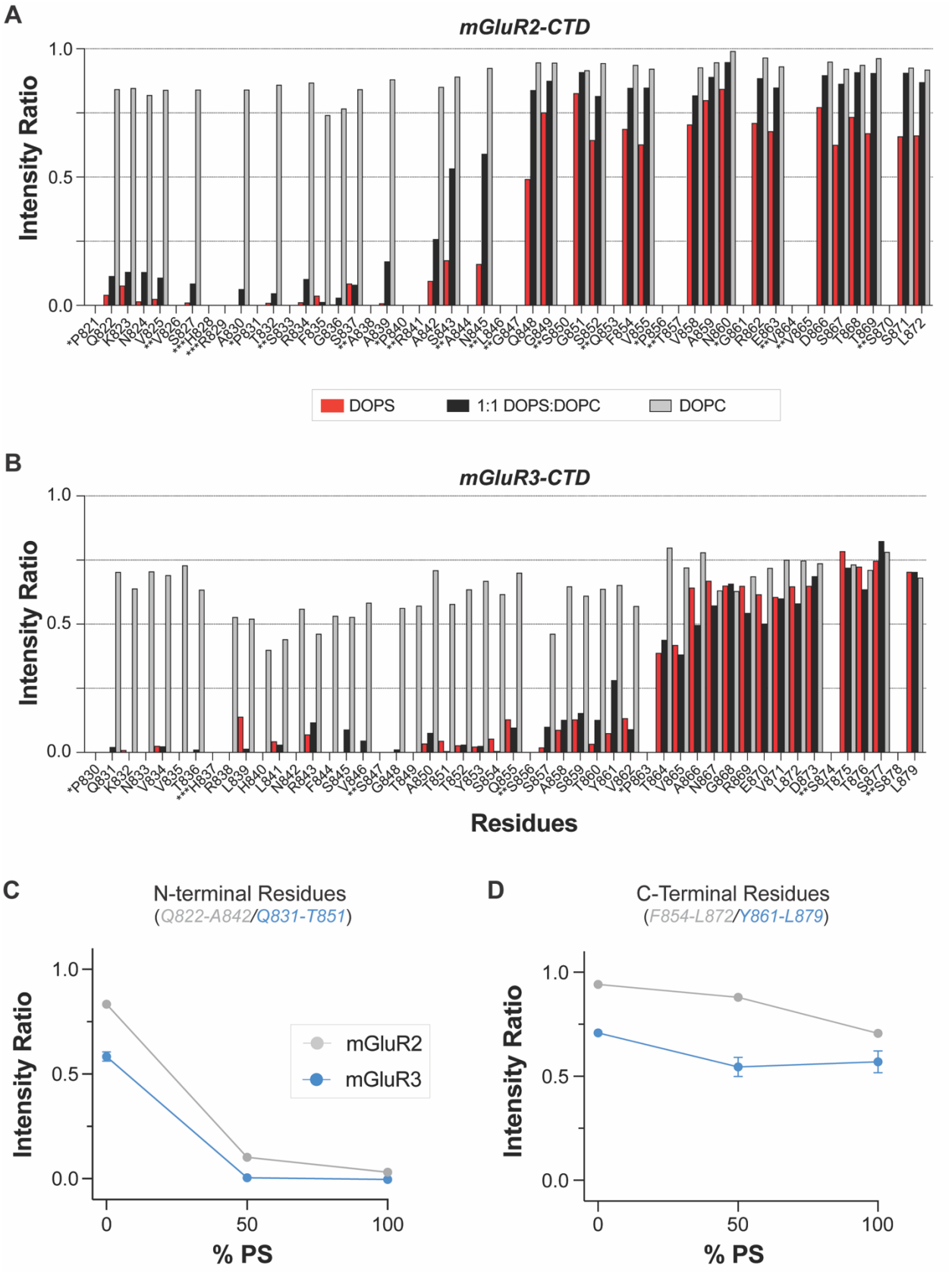

bioRxiv preprint doi: https://doi.org/10.1101/2023.08.16.553551; this version posted August 17, 2023. The copyright holder for this preprint (which was not certified by peer review) is the author/funder, who has granted bioRxiv a license to display the preprint in perpetuity. It is made available under aCC-BY-NC-ND 4.0 International license.

Figure 2: N-terminal regions of mGluR2 and 3 CTDs interact with negatively charged lipids. NMR intensity ratios for **(A)** mGluR2 and **(B)** mGluR3 from spectra collected with and without LUVs of three different lipid compositions. Prolines, which do not give rise to signals in ^{1}H-^{15}N HSQC spectra, are denoted by *, overlapping peaks for which values were not included by **, and residues not detected in the spectra by ***. **(C)** Averaged intensity ratios over the first ~20 residues (mGluR2 Q822-A842; mGluR3 Q831-T851) illustrate the lipid composition dependence of the interactions in this region (±s.e.m.). **(D)** Averaged intensity ratios over the last ~20 residues (mGluR2 Q853-L872; mGluR3 Y861-L879) illustrate the lack of lipid composition dependence of the interactions in this region (±s.e.m.).

bioRxiv preprint doi: https://doi.org/10.1101/2023.08.16.553551; this version posted August 17, 2023. The copyright holder for this preprint (which was not certified by peer review) is the author/funder, who has granted bioRxiv a license to display the preprint in perpetuity. It is made available under aCC-BY-NC-ND 4.0 International license.

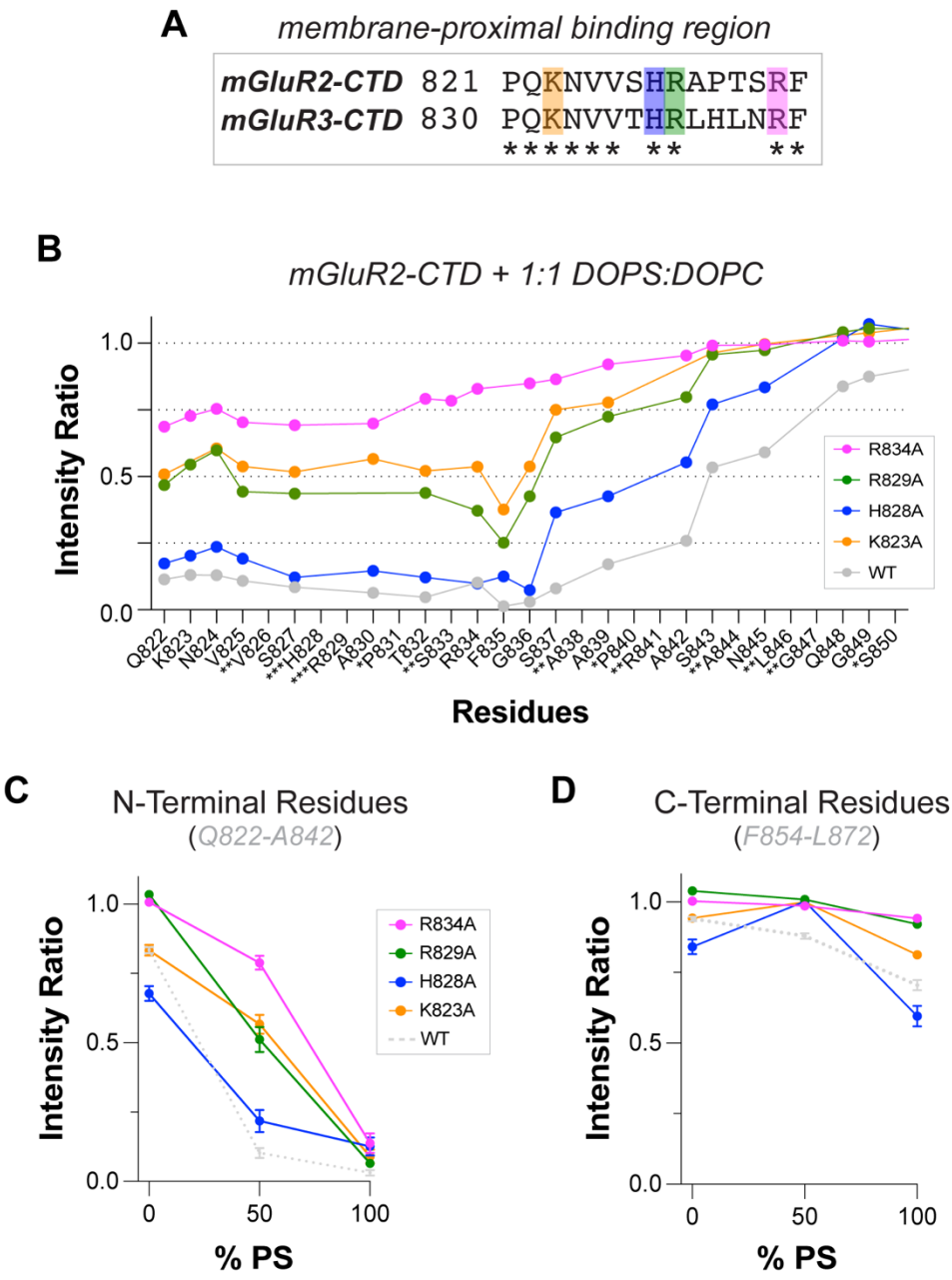

Figure 3: An N-terminal cluster of basic residues is critical for CTD membrane binding. (A) sequence alignment of the first 15 residues of the mGluR2 and mGluR3 CTDs highlighting conserved (*) and positively charged (highlighted) residues. **(B)** Intensity ratio plots of mGluR2 CTD constructs containing alanine substitutions for each of the four basic residues from spectra collected with and without LUVs containing a 1:1 mixture of DOPS:DOPC lipids. **(C)** Averaged intensity ratios over the first ~20 residues (Q822-A842) illustrate the regional effect of each mutation for LUVs of different lipid composition (±s.e.m.). **(D)** Averaged intensity ratios over the last ~20 residues (Q853-L872) illustrate the regional effect of each mutation for LUVs of different lipid composition (±s.e.m.).

bioRxiv preprint doi: https://doi.org/10.1101/2023.08.16.553551; this version posted August 17, 2023. The copyright holder for this preprint (which was not certified by peer review) is the author/funder, who has granted bioRxiv a license to display the preprint in perpetuity. It is made available under aCC-BY-NC-ND 4.0 International license.

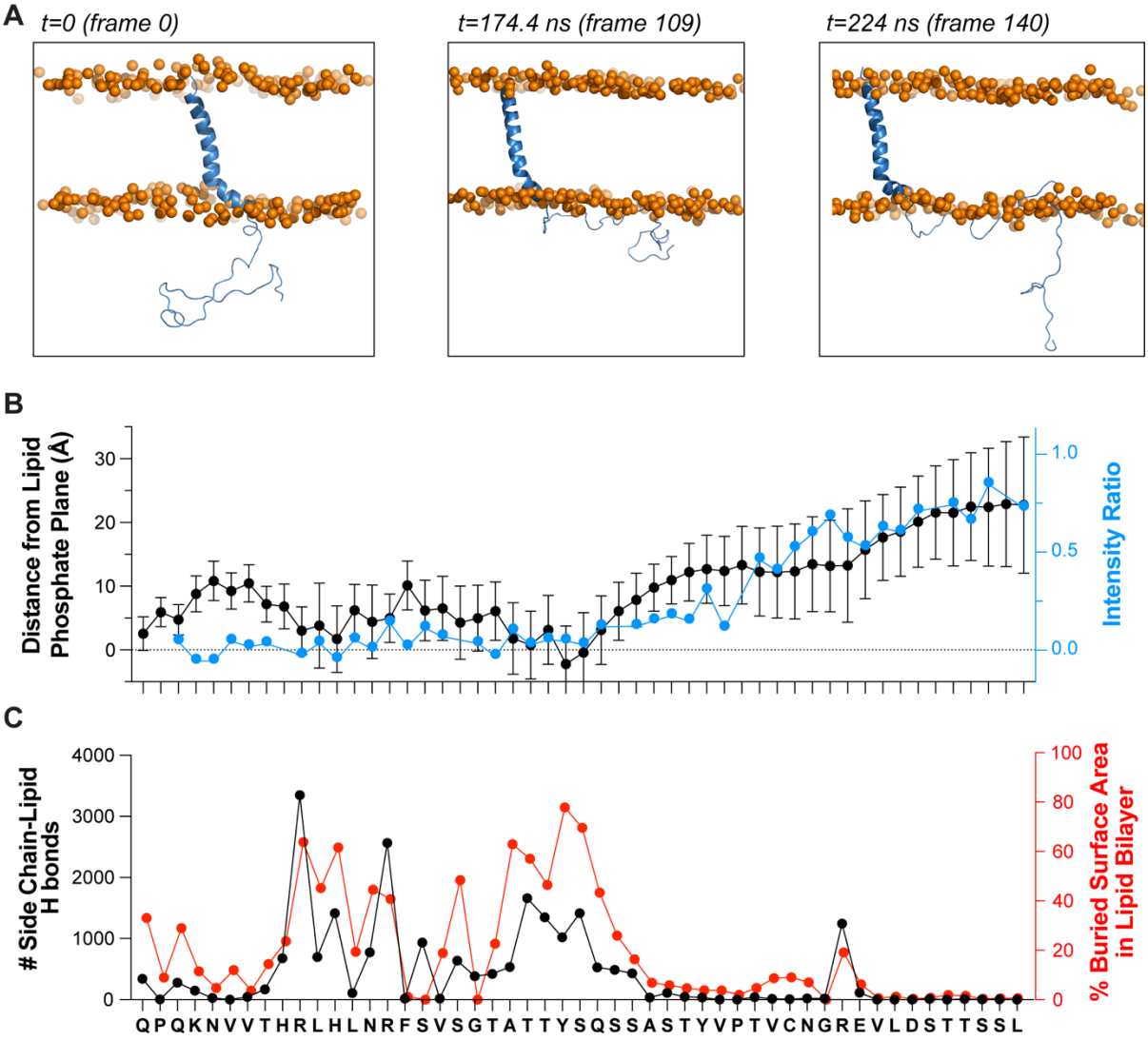

Figure 4: Molecular dynamics simulations reveal multi-modal membrane interactions of the intrinsically disordered mGluR3-CTD. (A) Snapshots of mGluR3 TM7-CTD replica 6 trajectory, highlighting three conformations of the CTD: the beginning of the simulation with no membrane contacts (t=0, left), a highly extended membrane-binding mode (t=174.4 ns, middle), and a partially extended binding (t=224 ns, right) **(B)** Comparison of the intensity ratios for the mGluR3 CTD in the presence of 1:1 DOPS:DOPC LUVs (blue, right axis) with the average distance of each residue from the lipid phosphate plane over the course of the simulation (black, left axis). **(C)** Interactions between CTD residue side chains and lipids: Left, black – total number of hydrogen bonds between each side chain and lipid headgroups; Right, red – average percent buried surface area of each side chain in the membrane.

bioRxiv preprint doi: https://doi.org/10.1101/2023.08.16.553551; this version posted August 17, 2023. The copyright holder for this preprint (which was not certified by peer review) is the author/funder, who has granted bioRxiv a license to display the preprint in perpetuity. It is made available under aCC-BY-NC-ND 4.0 International license.

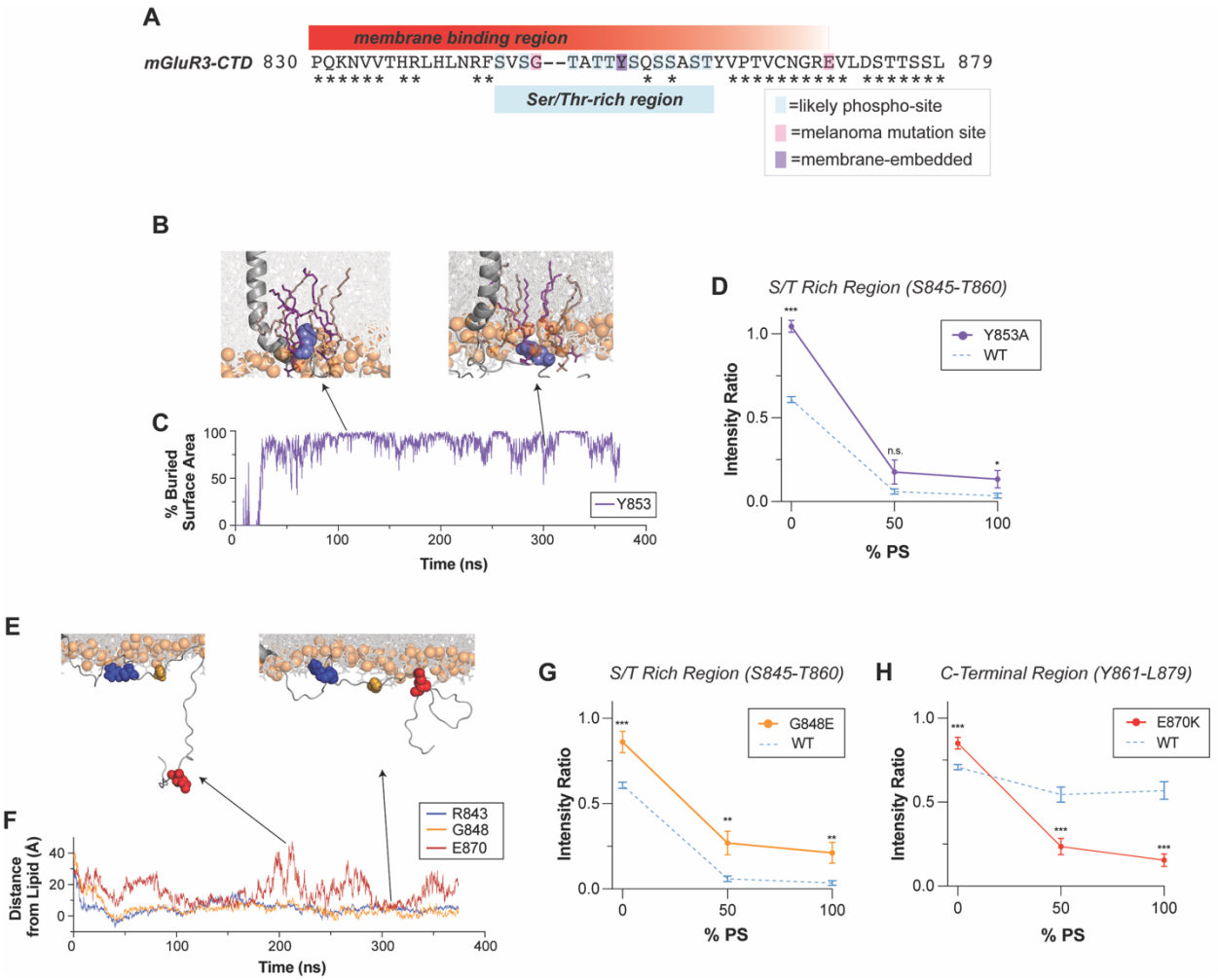

Figure 5: Membrane interactions of the S/T-rich region of the mGluR3 CTD is modulated by mutation of a key residue and by cancer mutations. (A) mGluR3-CTD sequence annotated with the NMR- and MD-determined membrane binding region and the overlapping Ser/Thr-rich region (* denotes residues conserved in mGluR2). **(B)** Snapshots of residue Y853 (shown as slate blue spheres) in membrane-embedded and membrane-associated positions (from MD replica 6). Lipid phosphates are shown as transparent orange spheres and lipid chains in contact with Y853 are shown in stick representation (DOPS in magenta and DOPC in salmon). Remaining lipids are shown in transparent gray and the protein backbone is shown in gray in cartoon representation. **(C)** Percent buried surface area of Y853 in the lipid bilayer plotted as a function of time in MD replica 6. **(D)** Comparison of the averaged integrated NMR intensity ratios of WT mGluR3-CTD (dotted blue) with Y853A mGluR3-CTD taken over the S/T-rich region (S845-T860) as a function of LUV lipid composition (±s.e.m.; Wilcoxon test; *p<0.05, ***p<0.001, n.s. p≥0.05). **(E)** Snapshots of residues R843 (blue), G848 (orange) and E870 (red) at different time points during the time course of MD replica 6 showing prolonged membrane-association of R843 and G848 and fluctuating membrane-association of E870 (side chains shown as spheres colored as in **(F)** below; otherwise rendered and colored as above in **(B)**). **(F)** Position of side chains R843, G848, and E870 relative to the phosphate plane of the membrane (see methods) throughout the time course of MD replica 6. **(G)** Comparison of the averaged NMR intensity ratios of WT mGluR3-CTD (dotted blue) with melanoma-associated mutations G848E mGluR3-CTD (orange) taken over the S/T-rich region (S845-T860) as a function of LUV lipid composition (±s.e.m.; Wilcoxon test; **p<0.01, ***p<0.001). **(H)** and E870K mGluR3-CTD (red) taken over the last 19 residues (Y861-L879) as a function of LUV lipid composition (±s.e.m.; Wilcoxon test; ***p<0.001).

bioRxiv preprint doi: https://doi.org/10.1101/2023.08.16.553551; this version posted August 17, 2023. The copyright holder for this preprint (which was not certified by peer review) is the author/funder, who has granted bioRxiv a license to display the preprint in perpetuity. It is made available under aCC-BY-NC-ND 4.0 International license.

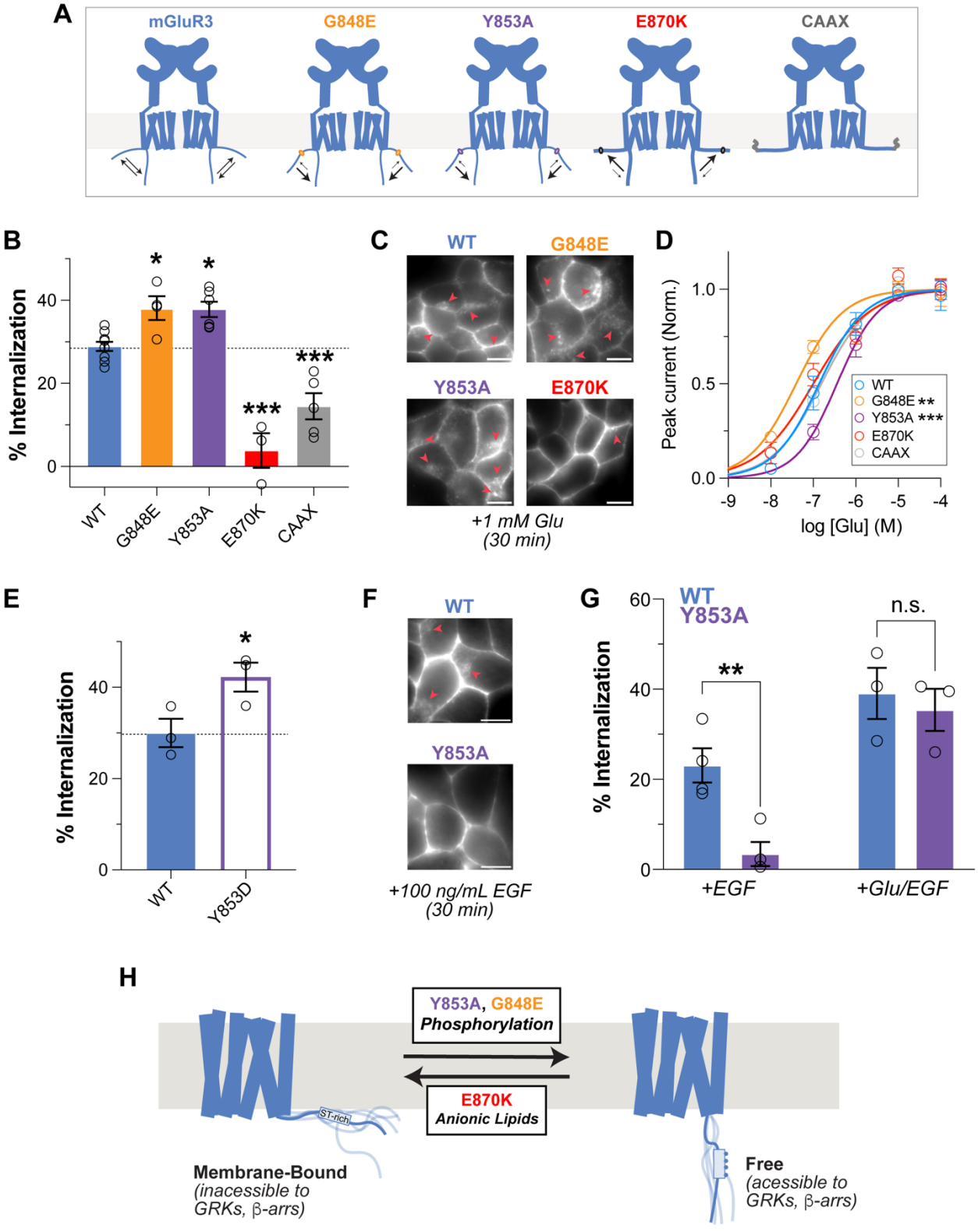

Figure 6: CTD mutations that alter membrane binding affect mGluR3 internalization and function. **(A)** Schematics of mGluR3 CTD mutational positions and their effects on mGluR3-CTD free vs. membrane bound equilibrium. Larger arrows show the direction in which each variant perturbs the equilibrium. **(B)** Quantification of the extent of receptor internalization for each mGluR3 variant (with dotted line denoting

bioRxiv preprint doi: https://doi.org/10.1101/2023.08.16.553551; this version posted August 17, 2023. The copyright holder for this preprint (which was not certified by peer review) is the author/funder, who has granted bioRxiv a license to display the preprint in perpetuity. It is made available under aCC-BY-NC-ND 4.0 International license.

mGluR3 WT internalization) (averaged internalization per day, 10-12 images per condition/day and 4-9 days per condition; One-Way ANOVA with multiple comparisons, * p<0.05 *** p<0.001). **(C)** Representative images of HEK 293T cells expressing SNAP-tagged mGluR3 variants incubated for 30 min with 1 mM Glu (red arrows represent internalized receptors; scale bar: 5 µm). **(D)** Glutamate dose response curves for mGluR3 variants in a patch-clamp experiment using GIRK currents as a reporter for mGluR3 G-protein activation (EC50: WT = 136.9 ± 26.9 nM, G848E = 44.2 ± 8.6 nM, Y853A = 417.8 ± 64.8 nM, E870K = 101.6 ± 21.7 nM, CAAX = 156.9 ± 42.8 nM; F-test of EC50 shifts; **p<0.01, ***p<0.001). **(E)** Quantification of the extent of recepor internalization of WT mGluR3 vs. Y853D phospho-mimetic mutant (averaged internalization of 10 images per condition/day across 3 days; t-test; *p<0.05. **(F)** Representative images of HEK293T cells expressing SNAP-tagged mGluR3 WT vs Y853A treated with 100 ng/ml EGF for 30 min (red arrows represent internalization; scale bar: 5 µm). **(G)** Quantification of the extent of internalization for mGluR3 WT vs Y853A mutant in EGF or Glu+EGF incubated conditions (averaged internalization per day, 10 images condition/day and 3-4 days per condition; t-test, **p<0.01 , n.s. p≥0.05). **(H)** Working model of mGluR3-CTD free vs. membrane bound equilibrium and changes that favor the less accessible membrane-bound (E870K, anionic lipids) or the more accessible free (Y853A, G848E, phosphorylation) state.

bioRxiv preprint doi: https://doi.org/10.1101/2023.08.16.553551; this version posted August 17, 2023. The copyright holder for this preprint (which was not certified by peer review) is the author/funder, who has granted bioRxiv a license to display the preprint in perpetuity. It is made available under aCC-BY-NC-ND 4.0 International license.

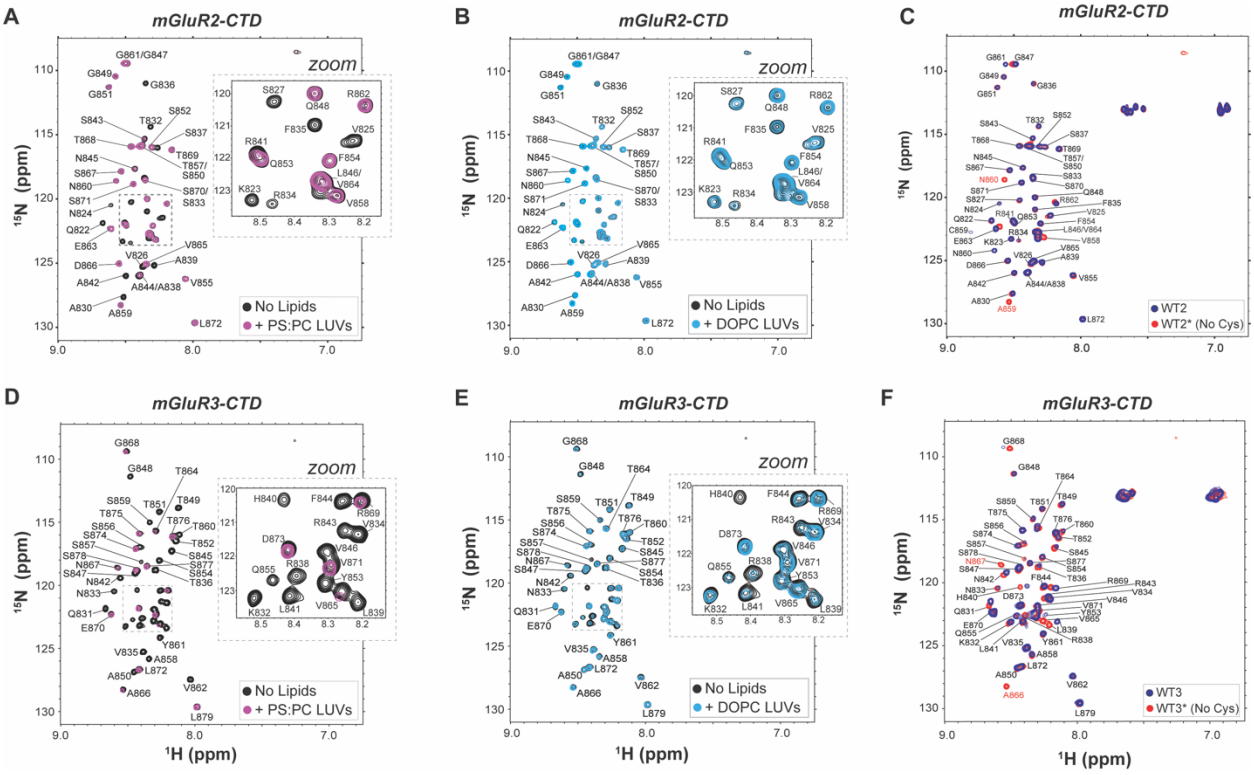

Figure S1: NMR spectra of mGluR2 and mGluR3 with LUVs of different compositions and of WT and cysteine-free variants. ^{1}H-^{15}N HSQC spectra of mGluR2 **(A,B)** and mGluR3 **(D,E)** CTDs in the presence (purple or light blue) and absence (black) of LUVs comprised of 1:1 DOPS:DOPC **(A,D)** or DOPC **(B,E)** with zoomed insets of crowded regions highlighting loss of signal of specific residues in the presence of LUVs. ^{1}H-^{15}N HSQC spectra of **(C)** mGluR2 WT (dark blue) and WT* (C859A mutant, red) CTD and **(F)** mGluR3 WT (dark blue) and WT* (C866A mutant, red) CTD. Chemical shift changes are confined to residues in the immediate vicinity of the mutations.

bioRxiv preprint doi: https://doi.org/10.1101/2023.08.16.553551; this version posted August 17, 2023. The copyright holder for this preprint (which was not certified by peer review) is the author/funder, who has granted bioRxiv a license to display the preprint in perpetuity. It is made available under aCC-BY-NC-ND 4.0 International license.

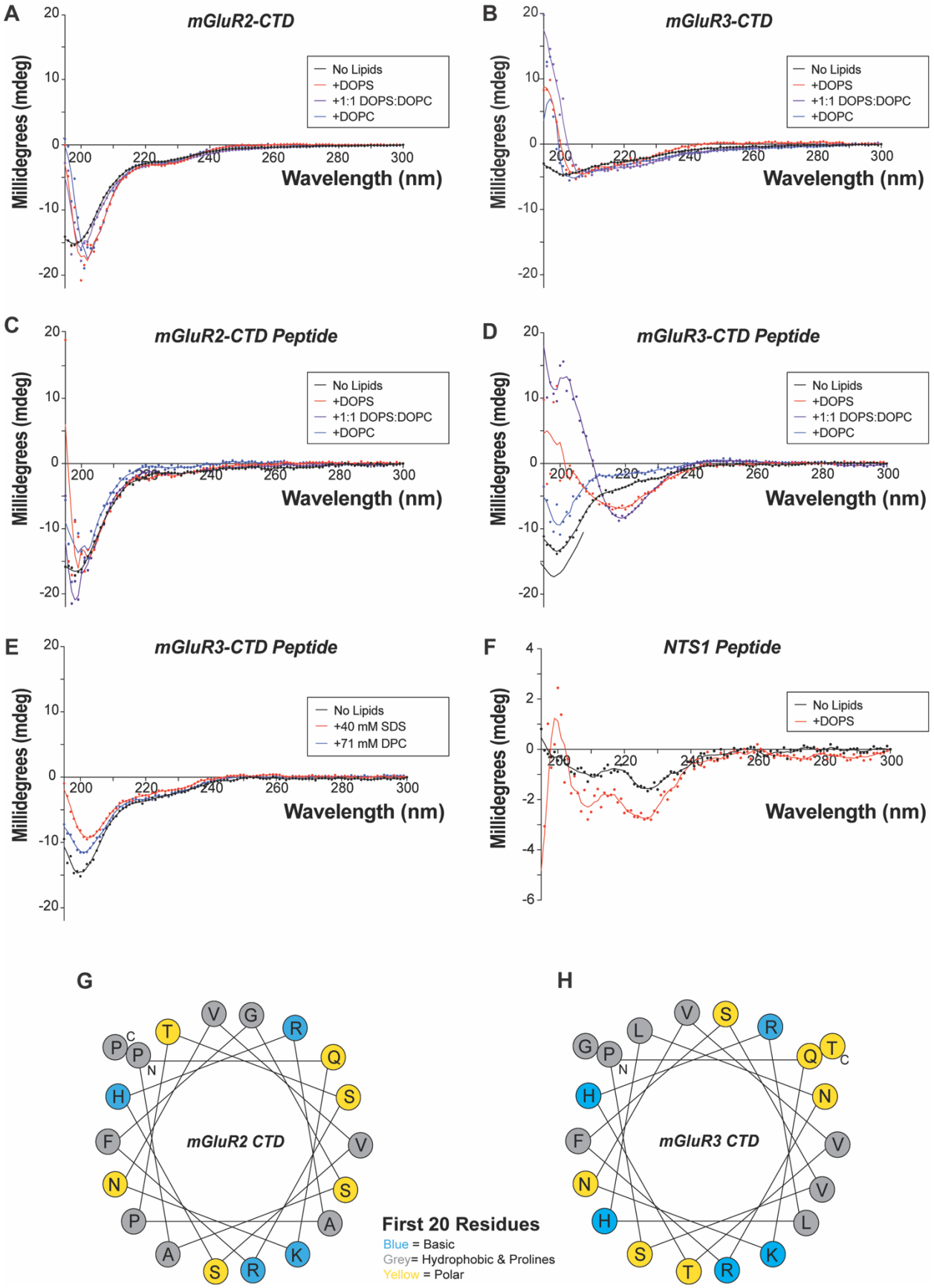

bioRxiv preprint doi: https://doi.org/10.1101/2023.08.16.553551; this version posted August 17, 2023. The copyright holder for this preprint (which was not certified by peer review) is the author/funder, who has granted bioRxiv a license to display the preprint in perpetuity. It is made available under aCC-BY-NC-ND 4.0 International license.

Figure S2: Secondary structure analysis of mGluR CTDs using CD. Circular dichroism spectra of the mGluR2 **(A)** and mGluR3 **(B)** CTD and mGluR2 **(C)** and mGluR3 **(D)** peptides encompassing the NMR determined binding region (first 23 residues) in the absence of LUVs (black) or in the presence of 10 mM, 100 nm diameter **(A)** or 50 nm diameter **(B-D)** DOPC (blue), 1:1 DOPS:DOPC (purple) or DOPS (red) LUVs under conditions where NMR indicates no (DOPC) or complete (DOPS or 1:1 DOPS:DOPC) CTD binding. Note that for **(A)** the sudden increase in signal below 205 nm results from increased scattering due to the use of 100 nm diameter LUVs in these samples. For **(D)** the spectra suggest a degree of β-strand formation, possibly due to intermolecular interactions caused by the limited solubility of this peptide **(E)** CD spectra of mGluR3 peptides encompassing the NMR determined binding region (first 23 residues) in the absence (black) or presence of 40 mM SDS (red) or 71 mM DPC (blue). **(F)** CD spectra of NTSR1 peptide free in solution (black) and in the presence of 10 mM 50 nm diameter DOPS LUVs (red). **(G,H)** Helical wheel representations of the first 20 residues of the mGluR2 **(G)** and mGluR3 **(H)** CTD illustrating the lack of clear amphipathic character (basic residue in blue, polar residues in yellow, apolar residues in white).

bioRxiv preprint doi: https://doi.org/10.1101/2023.08.16.553551; this version posted August 17, 2023. The copyright holder for this preprint (which was not certified by peer review) is the author/funder, who has granted bioRxiv a license to display the preprint in perpetuity. It is made available under aCC-BY-NC-ND 4.0 International license.

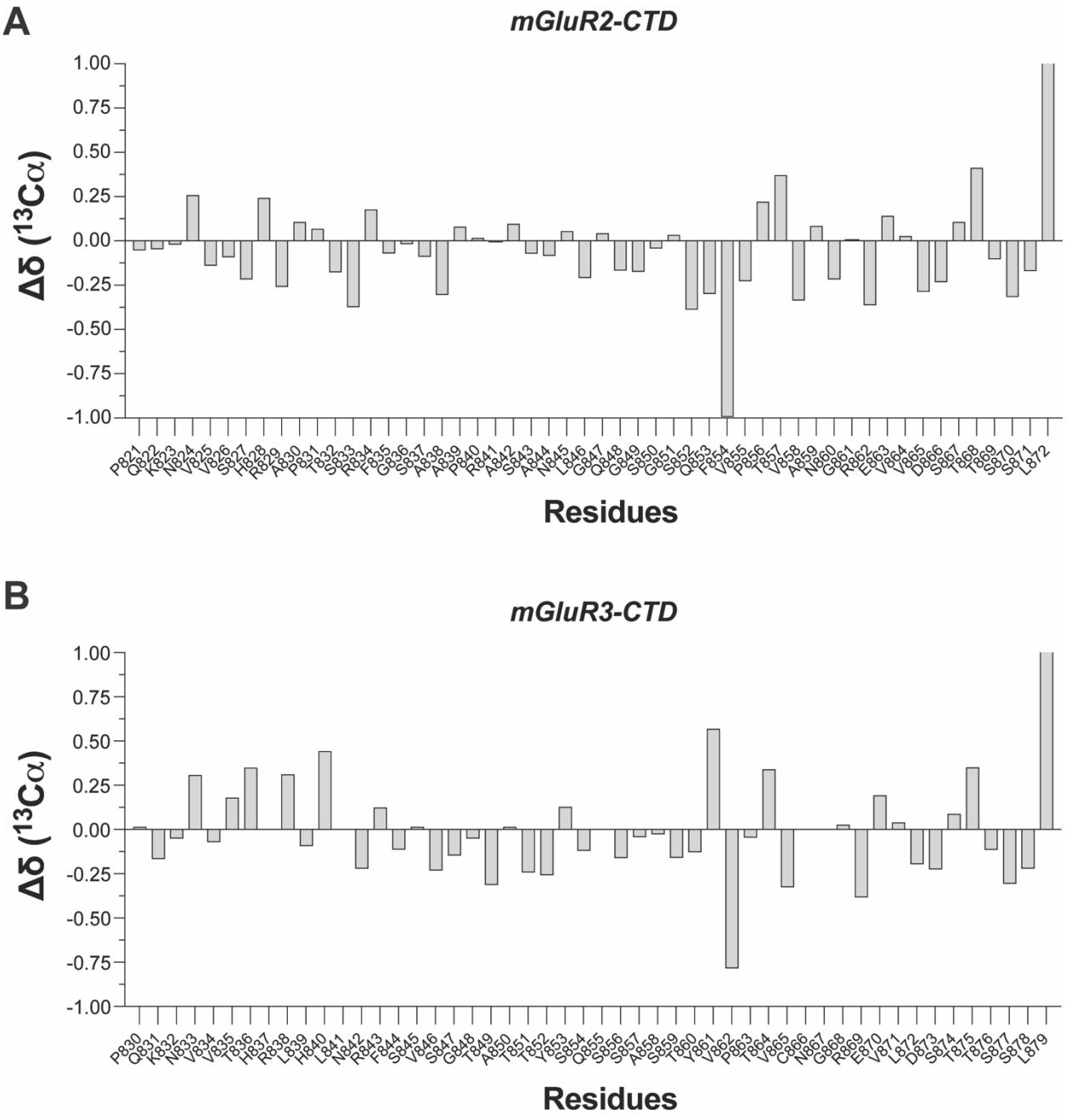

Figure S3: Secondary structure analysis of mGluR CTDs using NMR. Secondary C_α chemical shifts for the mGluR2 **(A)** and mGluR3 **(B)** CTDs free in solution. Positive/negative deviations greater than 1.0 PPM indicate a propensity for helical/β-strand secondary structure, respectively.

bioRxiv preprint doi: https://doi.org/10.1101/2023.08.16.553551; this version posted August 17, 2023. The copyright holder for this preprint (which was not certified by peer review) is the author/funder, who has granted bioRxiv a license to display the preprint in perpetuity. It is made available under aCC-BY-NC-ND 4.0 International license.

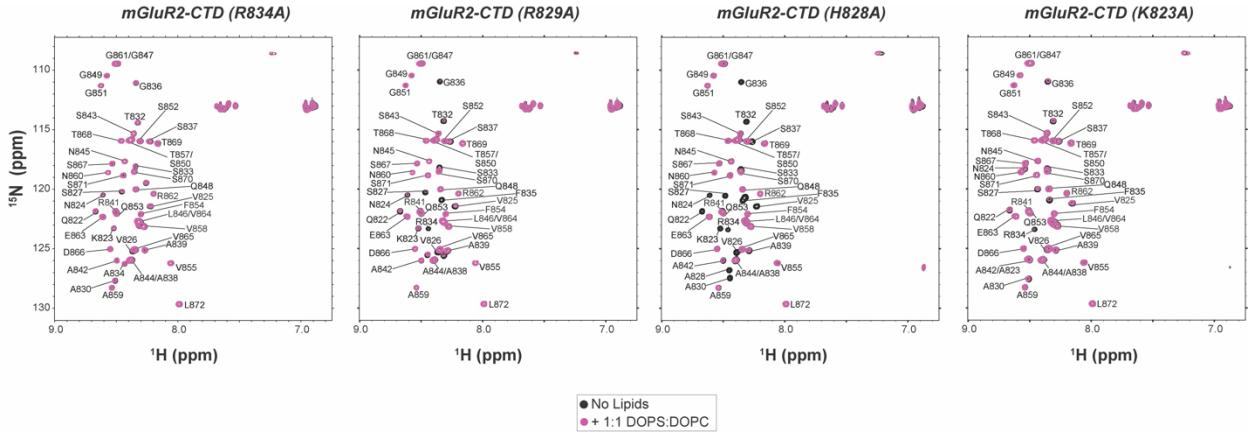

Figure S4: Mutating positively charged residues impacts CTD-membrane interactions. ^{1}H-^{15}N HSQC spectra of mGluR2 CTD variants in the presence (purple) and absence (black) of 100 nm LUVs comprised of 1:1 DOPS:DOPC.

bioRxiv preprint doi: https://doi.org/10.1101/2023.08.16.553551; this version posted August 17, 2023. The copyright holder for this preprint (which was not certified by peer review) is the author/funder, who has granted bioRxiv a license to display the preprint in perpetuity. It is made available under aCC-BY-NC-ND 4.0 International license.

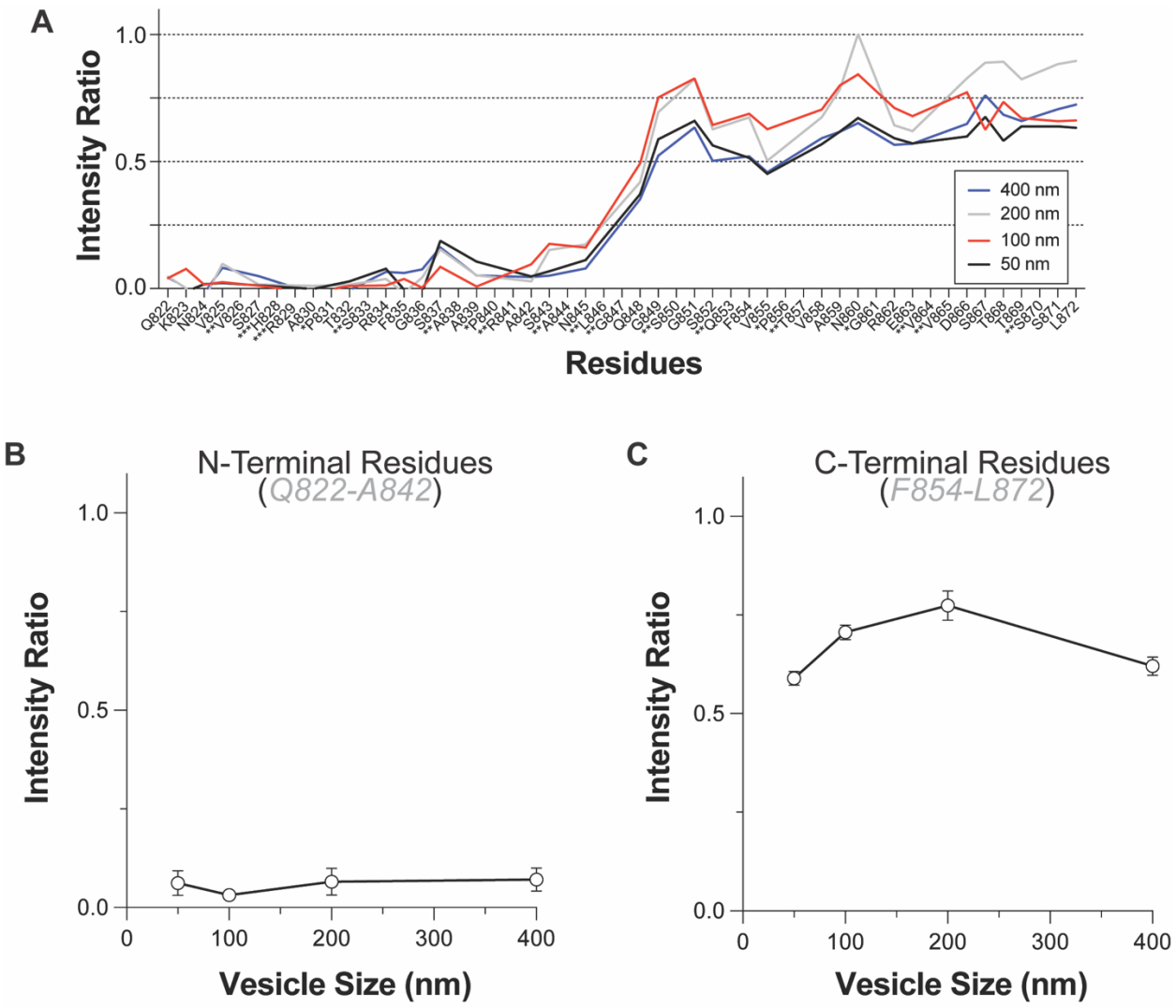

Figure S5: mGluR CTDs LUVs binding as a function of vesicle size. (A) NMR intensity ratio plots for the mGluR2-CTD in the presence of DOPS LUVs of varying diameter. **(B)** Averaged intensity ratios over the first ~20 residues (Q822-A842) (±s.e.m.). **(C)** Averaged intensity ratios over the last ~20 residues (Q853-L872) (±s.e.m.).

bioRxiv preprint doi: https://doi.org/10.1101/2023.08.16.553551; this version posted August 17, 2023. The copyright holder for this preprint (which was not certified by peer review) is the author/funder, who has granted bioRxiv a license to display the preprint in perpetuity. It is made available under aCC-BY-NC-ND 4.0 International license.

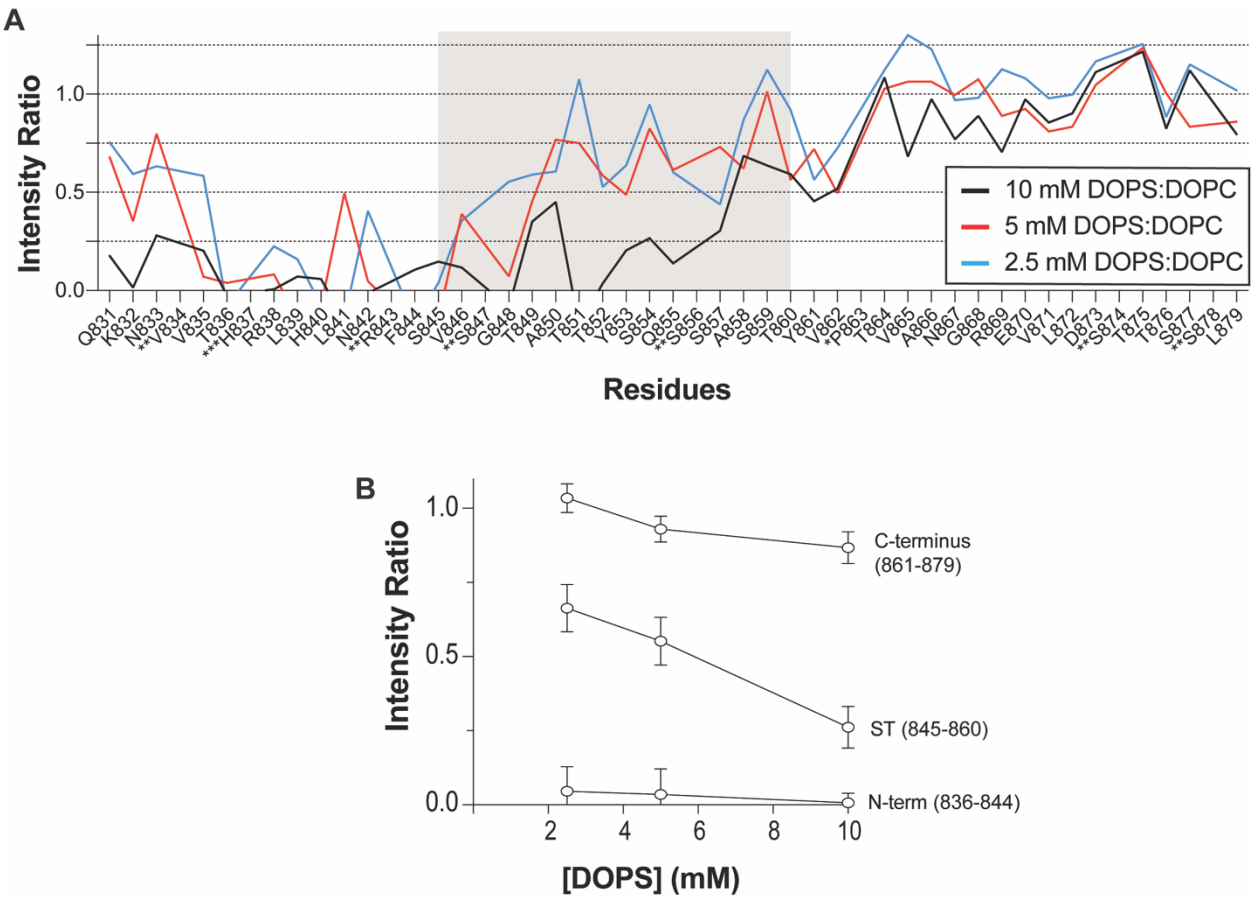

Figure S6: Lipid titration identifies weaker and stronger interaction regions of the mGluR3 CTD. **(A)** NMR intensity ratios for the mGluR3-CTD in the presence of varying concentrations of 1:1 DOPS:DOPC LUVs. **(B)** Average intensity ratios over different regions of the mGluR3 CTD highlight the greater sensitivity of the S/T-rich region to lipid concentration (±s.e.m.).

bioRxiv preprint doi: https://doi.org/10.1101/2023.08.16.553551; this version posted August 17, 2023. The copyright holder for this preprint (which was not certified by peer review) is the author/funder, who has granted bioRxiv a license to display the preprint in perpetuity. It is made available under aCC-BY-NC-ND 4.0 International license.

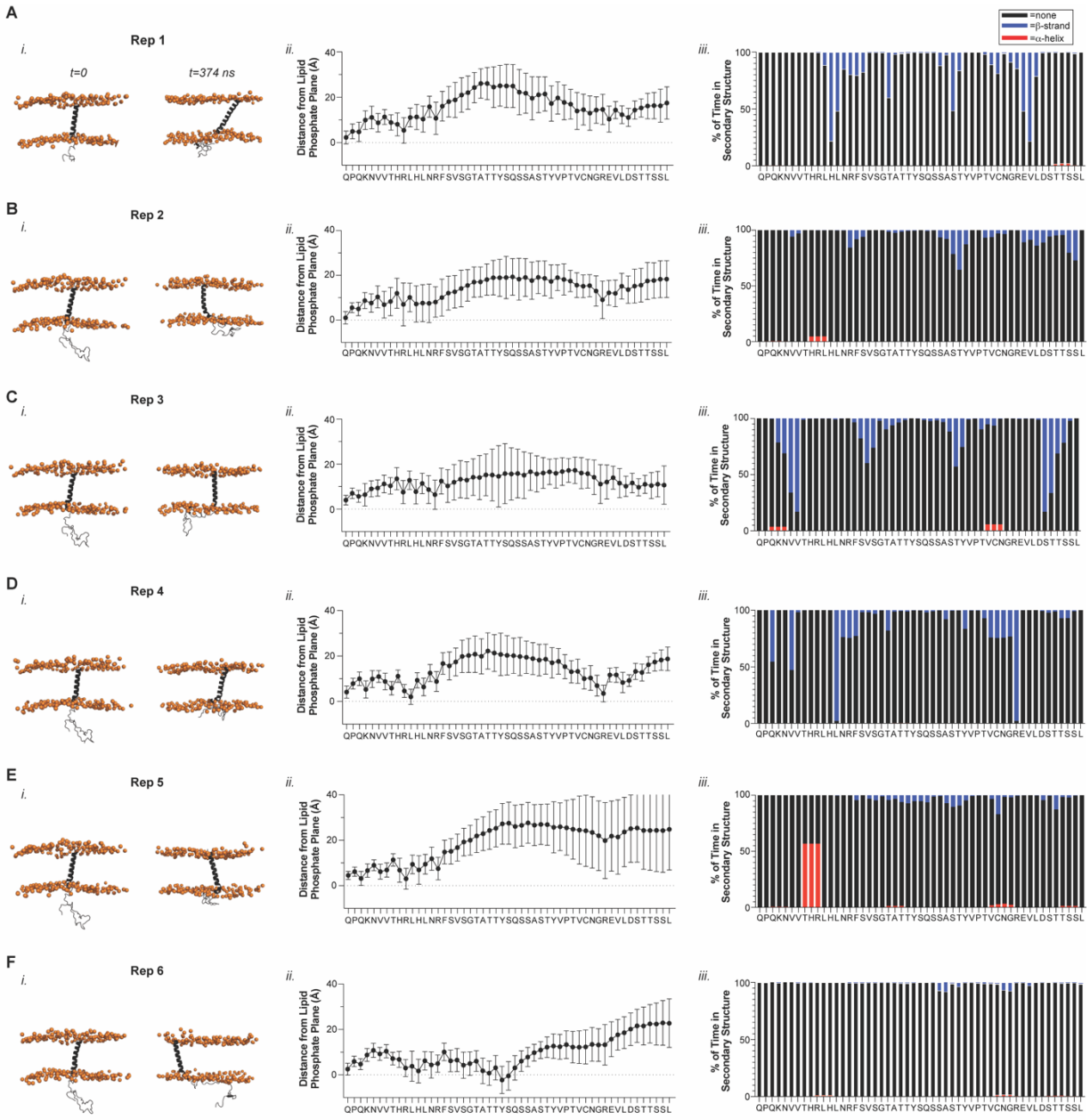

Figure S7: MD simulations capture mGluR3 CTD-membrane interactions and confirm absence of regular secondary structure. (**A-F)** (i, left) snapshots of starting and ending frames of each MD simulation replica of the mGluR3 TM7-CTD construct with the protein shown in black cartoon representation and lipid phosphates as orange spheres; (ii, middle) average residue distance from the phosphate plane in each replica with error bars corresponding to standard deviations; (iii, right) Percent of trajectory frames for each CTD residue residing in disordered (black), helical (red), or beta-sheet (blue) secondary structure during each replica trajectory.

bioRxiv preprint doi: https://doi.org/10.1101/2023.08.16.553551; this version posted August 17, 2023. The copyright holder for this preprint (which was not certified by peer review) is the author/funder, who has granted bioRxiv a license to display the preprint in perpetuity. It is made available under aCC-BY-NC-ND 4.0 International license.

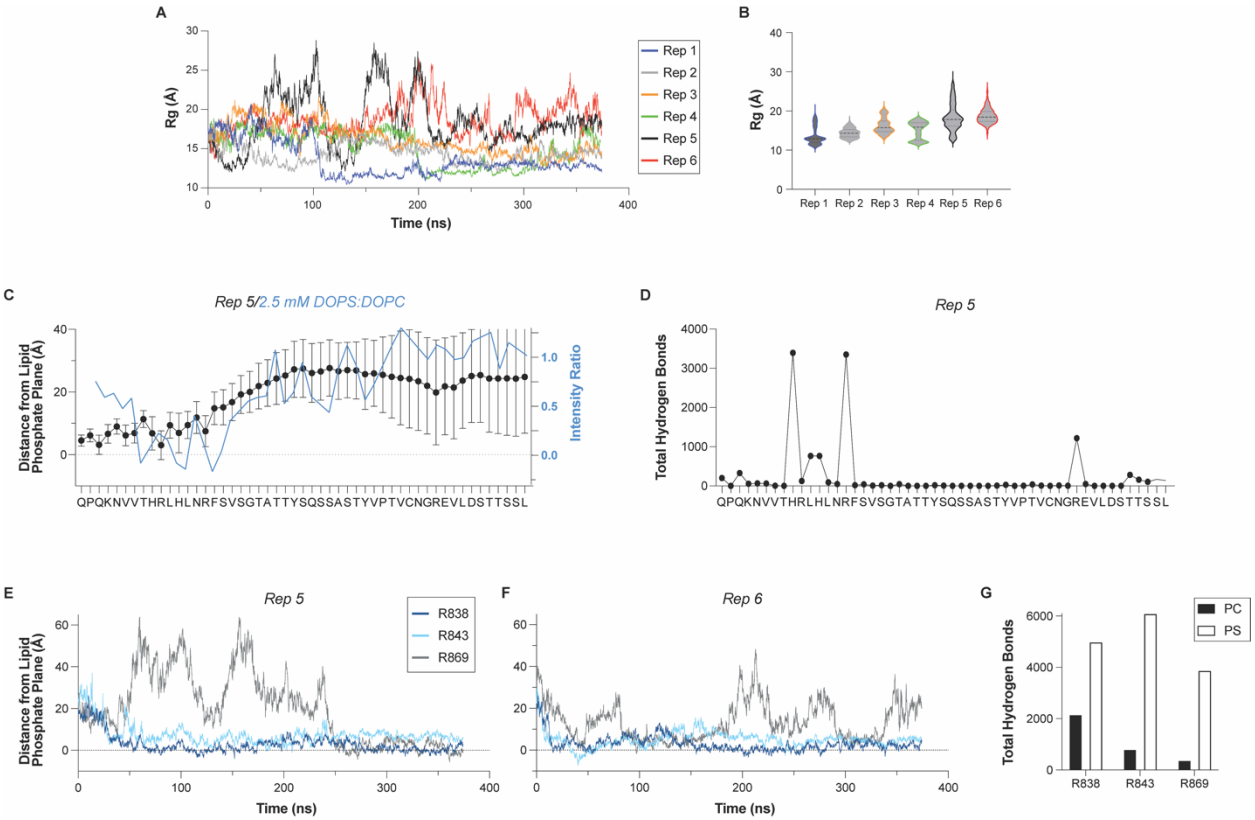

Figure S8: Comparison and analysis of MD simulation replicas. (A) Radius of gyration for the CTD (residues 830-879) during the course of each MD replica. **(B)** Violin plots of radii of gyration for each MD replica annotated with mean (thick dotted line) and one standard deviation (thin dotted lines). **(C)** Comparison of the intensity ratios for the mGluR3 CTD in the presence of 2.5 mM 1:1 DOPS:DOPC LUVs (blue, right axis) with the average distance of each residue from the lipid phosphate plane over the course of the MD replica 5 (black, left axis). Note that the discrepancy at the very N-terminus may arise from the CTD being membrane-anchored in the simulations but not in the NMR experiments. **(D)** Total number of hydrogen bonds between side chains of each CTD residue and DOPS lipid headgroups from MD replica 5. **(E, F)** Position of arginine side chains relative to the phosphate plane of the membrane (see methods) throughout the time course of MD replica 5 **(E)** and 6 **(F)**. **(G)** Total number of hydrogen bonds summed from MD replicas 5 and 6 between each arginine side chain and DOPC or DOPS lipid headgroups, highlighting the preference for interactions with negatively charged PS headgroups.

bioRxiv preprint doi: https://doi.org/10.1101/2023.08.16.553551; this version posted August 17, 2023. The copyright holder for this preprint (which was not certified by peer review) is the author/funder, who has granted bioRxiv a license to display the preprint in perpetuity. It is made available under aCC-BY-NC-ND 4.0 International license.

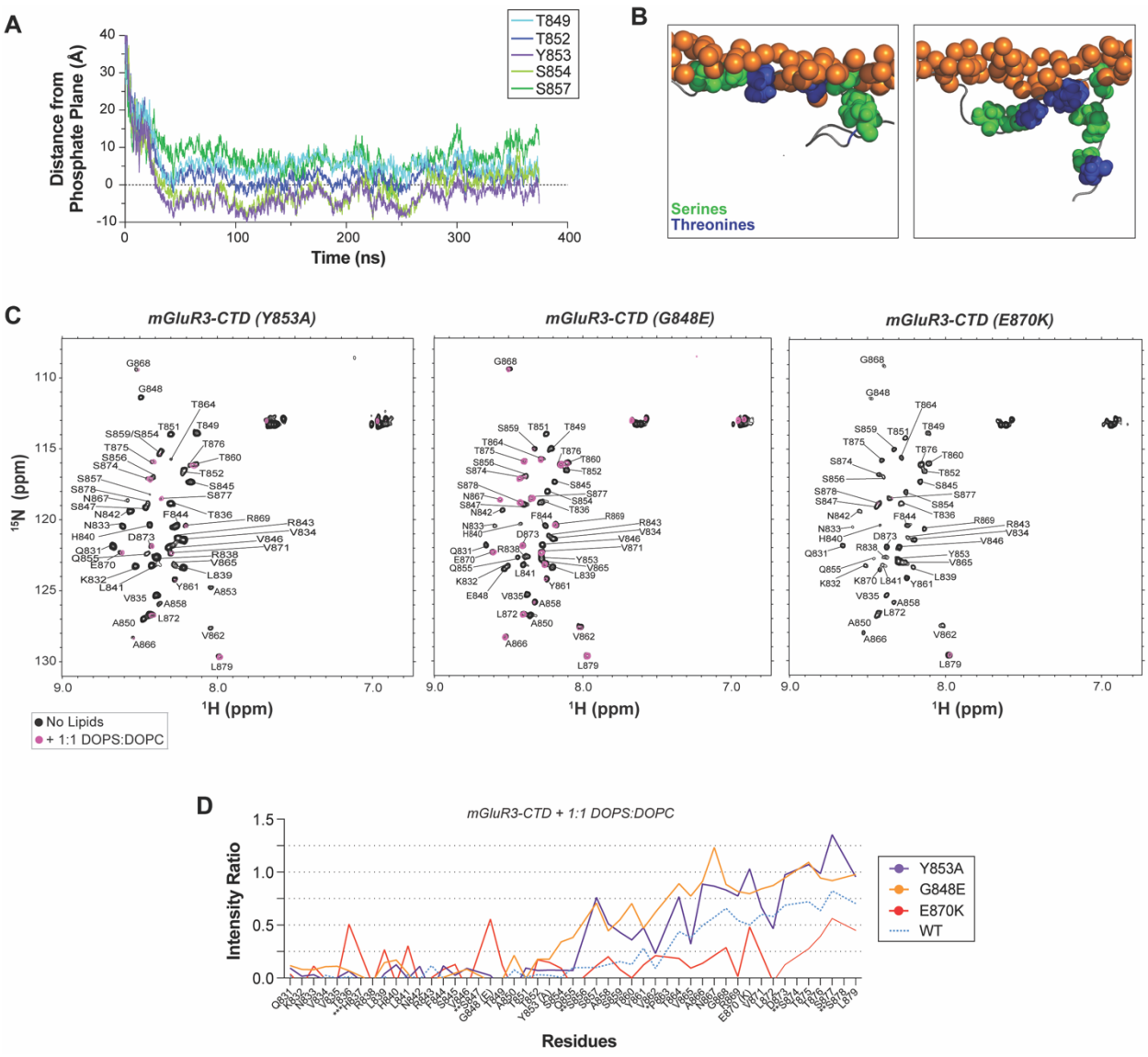

Figure S9: Y853 and cancer-associated mutations modulate membrane binding of the mGlur3 S/T-rich region. (A) Distance from phosphate plane of side chains in the S/T-rich region as a function of time for Y853 and nearby S/T residues in MD replica 6. **(B)** Snapshots of S/T residues in the S/T-rich region position relative to the membrane highlighting the dynamics of the region during our simulations. Side chains are shown as spheres (Ser in green and Thr in blue) and lipid phosphates are shown as orange spheres. Protein backbone is in gray cartoon **(C)** ^{1}H-^{15}N HSQC spectra of mGluR3 CTD variants in the presence (purple) and absence (black) of 1:1 DOPS:DOPC. **(D)** NMR intensity ratios WT (dotted blue line), Y853A (purple), G848E (orange), and E870K (red) mGluR3-CTD in the presence of 10 mM 100 nm diameter LUVs comprised of 1:1 DOPS:DOPC 100 nm LUVs.

bioRxiv preprint doi: https://doi.org/10.1101/2023.08.16.553551; this version posted August 17, 2023. The copyright holder for this preprint (which was not certified by peer review) is the author/funder, who has granted bioRxiv a license to display the preprint in perpetuity. It is made available under aCC-BY-NC-ND 4.0 International license.

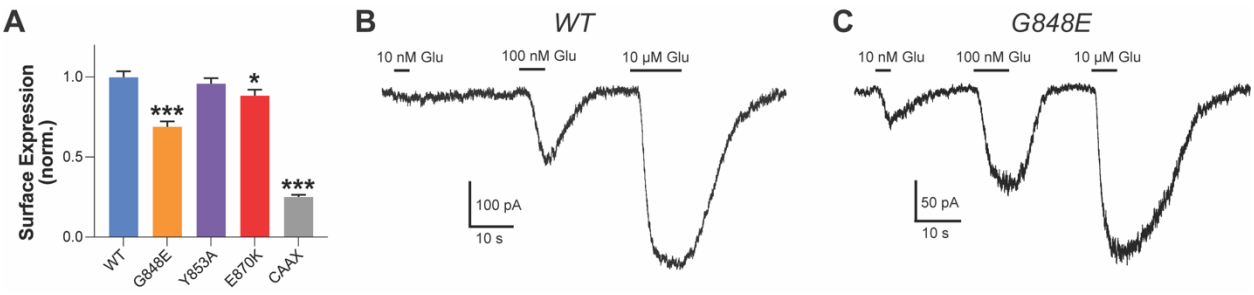

Figure S10: Surface expression of CTD-mutants and functional effects of G848E on mGluR3 activity. **(A)** Surface expression quantification for all the mutants tested in the study (One-way ANOVA with multiple comparisons; * $p<0.05$, *** $p<0.001$. **(B-C)** Representative traces of evoked GIRK potassium currents after mGluR3 activation by different doses of glutamate (10 nM, 100 nM and 10 µM) in WT **(B)** and G848E mutant **(C).**